JOURNAL OF PETROLOGY | VOLUME 51 | NUMBER 12 | PAGES 2489–2514 | 2010 | doi:10.1093/petrology/egq065

Prograde *P–T* Evolution of a Lawsonite Eclogite from the Monviso Meta-ophiolite (Western Alps): Dehydration and Redox Reactions during Subduction of Oceanic FeTi-oxide Gabbro

CHIARA GROPPO* AND DANIELE CASTELLI

DEPARTMENT OF MINERALOGICAL AND PETROLOGICAL SCIENCES, UNIVERSITY OF TORINO, VIA VALPERGA CALUSO 35, I-10125, TORINO, ITALY

RECEIVED FEBRUARY 8, 2010; ACCEPTED SEPTEMBER 22, 2010
ADVANCE ACCESS PUBLICATION NOVEMBER 18, 2010

Lawsonite eclogites represent fossil records of processes occurring during subduction of cold- and fast-subducting slabs, and provide an opportunity to investigate the thermal and metamorphic evolution of palaeosubduction zones. Occurrences of lawsonite eclogites are rare because lawsonite is often replaced during exhumation. We report here, for the first time, the occurrence of a lawsonite eclogite from the Monviso meta-ophiolite (Western Alps), representing the product of the Alpine metamorphism of a FeTi-oxide gabbro. The prograde metamorphic evolution of this lawsonite eclogite has been investigated using the petrological approach of pseudosections. The reconstruction of its prograde P–T *evolution allowed us to monitor changes in chemical and physical properties (mineral assemblages and compositions, density, H_2O content, oxygen fugacity) during subduction. The pseudosection modelling suggests peak metamorphic conditions of* $T \geq 550^{\circ}C$, $P = 25$–26 *kbar, and a decrease in the thermal gradient during subduction from about* $9^{\circ}C\ km^{-1}$ *to less than* $7^{\circ}C\ km^{-1}$, *which may be interpreted as related to an increase in the subduction rate. During its prograde evolution, at a depth of about 65–70 km, the eclogite-facies metagabbro experienced a significant dehydration passing from the* $Grt_1 + Omp_1 + Lws + Chl + Qtz + Rt$ *assemblage (stage I) to the* $Grt_2 + Omp_2 + Tlc + Qtz + Rt$ *assemblage (stage II). The breakdown of lawsonite and chlorite caused the release of up to 3 wt % of* H_2O *and also of oxygen, as modelled by the redox equilibrium* $Lws + Qtz + Chl + Omp_1 = Grt + Omp_2 + H_2O + O_2$. *This redox-equilibrium represents the boundary between an earlier, more oxidized assemblage (stage I), stable at lower* T, *and a later, more reduced assemblage (stage II), stable at higher* T. *These results have possible implications for the understanding of the complex interactions between crust and mantle in subduction zones, especially in clarifying the processes locally involved in the oxidation of the mantle wedge overlying the subducting slab.*

KEY WORDS: *dehydration and redox reactions; lawsonite eclogite; prograde* P–T *path;* P–T *pseudosections; subduction*

INTRODUCTION

Detailed petrological studies of prograde metamorphism in meta-ophiolites can provide important insights into the evolution of palaeosubduction zones, in terms of (1) their thermal structures and evolution, and (2) devolatilization reactions and metamorphic transformations occurring in the subducting slabs.

Several studies of heat flux and seismic activity carried out on present-day subduction zones (e.g. Royden & Husson, 2006; Schellart *et al.*, 2007) have shown that, in general, fast-subducting slabs are characterized by low thermal gradients, whereas slow-subducting slabs have higher thermal gradients (e.g. Peacock & Wang, 1999). Changes in the thermal structure of a subduction zone

*Corresponding author. Telephone: +39 011 6705106. Fax: +39 011 6705128. E-mail: chiara.groppo@unito.it

may result from changes in the subduction rate, in turn related to the complex interplay between the density and geometry of the slab, and to the viscosity structure of the surrounding mantle (e.g. Royden & Husson, 2006). Variations in subduction rates are widely reported from currently active subduction zones and may be also inferred for palaeosubduction environments on the basis of a careful reconstruction of the P–T–(t) evolution of meta-ophiolites (e.g. Groppo *et al.*, 2009*a*).

Devolatilization reactions, fluid–rock interactions and metamorphic transformations occurring in subducting slabs play a key role in revealing the complex physical–chemical transformations of crust and mantle at convergent margins. Fluids released from the variably hydrated subducting slab are, in fact, considered as the primary source of volatiles for arc magmatism and fluid-induced seismicity (e.g. Hawkesworth *et al.*, 1993; Parkinson & Arculus, 1999; Clift *et al.*, 2001; Kerrick & Connolly, 2001*b*; Peslier *et al.*, 2002; Forneris & Holloway, 2003; Hacker *et al.*, 2003; Spandler *et al.*, 2004). The dehydration history of the mafic portion of the subducting slab has been widely explored by high-pressure experiments since the early 1990s (e.g. Pawley & Holloway, 1993; Peacock, 1993; Yaxley & Green, 1994; Poli & Schmidt, 1995; Liu *et al.*, 1996; Schmidt & Poli, 1998; Molina & Poli, 2000; Forneris & Holloway, 2003; Dasgupta *et al.*, 2004; Dasgupta & Hirschmann, 2006; Poli *et al.*, 2009). Theoretical modelling of stable mineral assemblages at given P–T conditions has alternatively been used (e.g. Kerrick & Connolly, 1998, 2001*a*, 2001*b*; Hacker *et al.*, 2003; Rüpke *et al.*, 2004). All these studies show that dehydration of the mafic portion of the subducting slab mainly occurs through continuous reactions that involve the breakdown of hydrated minerals at different depths. Although a significant fluid loss characterizes the shallowest portion of the subduction zone, variable amounts of H_2O are still retained in hydrous assemblages at greater depths (e.g. Poli & Schmidt, 1995; Kerrick & Connolly, 2001*b*; Hacker *et al.*, 2003; Poli *et al.*, 2009). Lawsonite is among the most important H_2O-reservoirs, being able to accommodate up to 11·5 wt % H_2O in its structure. Although lawsonite eclogites are predicted to be common at depths of 45–300 km in cold subduction zones (e.g. Poli & Schmidt, 1995; Kerrick & Connolly, 2001*b*; Hacker *et al.*, 2003), lawsonite seldom survives exhumation (e.g. Tsujimori *et al.*, 2006*a*; Ghent *et al.*, 2009) because its preservation requires that exhumation be accompanied by substantial cooling (e.g. Clarke *et al.*, 2006; Davis & Whitney, 2006, 2008). As a consequence, only about 10 lawsonite-eclogite localities are currently known in Phanerozoic orogenic belts (see Tsujimori *et al.*, 2006*b*, for a review).

In the Western Alps, the Monviso metamorphic ophiolite represents one of the best preserved relics of the oceanic lithosphere that formed during the opening of Mesozoic Western Alpine Tethys and underwent eclogite-facies metamorphism during Alpine subduction. Despite a number of papers devoted to the study of the magmatic protoliths and to the investigation of peak metamorphic conditions reached during Alpine subduction (Lombardo *et al.*, 1978; Philippot, 1988; Blake *et al.*, 1995; Messiga *et al.*, 1999; Schwartz *et al.*, 2000; Castelli *et al.*, 2002; Castelli & Lombardo, 2007), very few data are available so far on the prograde evolution of the Monviso meta-ophiolites.

In this study, we have investigated the prograde metamorphic evolution of a very well preserved eclogitized FeTi-oxide gabbro from the Monviso meta-ophiolite, using the petrological approach of isochemical P–T phase diagrams (or P–T pseudosections). The first peculiarity of this eclogite is the occurrence of lawsonite preserved in the prograde cores of both garnet and omphacite. These findings, reported here for the first time for the whole Monviso meta-ophiolite, represent an important contribution to the understanding of subduction and exhumation processes of meta-ophiolites of the Western Alps. The second peculiarity of the studied sample is its Fe-rich bulk composition, which allowed the development of Fe-rich garnet and omphacite, both characterized by a strong prograde chemical zonation, with iron in both divalent and trivalent oxidation states. Petrological modelling of the studied sample, in the MnNCFMASTHO model system, has allowed us to:

(1) reconstruct the prograde evolution of the Basal Serpentinite Unit from the Monviso meta-ophiolite, not yet investigated so far; the obtained P–T trajectory, which lies inside the lawsonite eclogite-facies field, gives information about the thermal structure of the palaeosubduction zone, characterized by a decrease in the thermal gradient from 9 to 6–7°C km^{-1};
(2) monitor changes in chemical and physical properties (mineral assemblages, density, H_2O content) during subduction; we have investigated the main devolatilization reactions responsible for the dehydration of the metagabbro, and the consequences of the dehydration process on the mineral assemblages and zoning;
(3) obtain information about the redox reactions occurring in the metagabbro during subduction, with possible implication for the understanding of the complex interaction between crust and mantle in subduction zones.

GEOLOGICAL SETTING

The Monviso metamorphic ophiolite is a composite body, structurally sandwiched between the underlying Dora–Maira Massif and the other, dominantly metasedimentary, units of the ocean-derived Piedmont Zone (Fig. 1a). It is one of the best preserved relics of the oceanic crust in the Western Alps that formed between *c.* 170 and *c.* 150 Ma

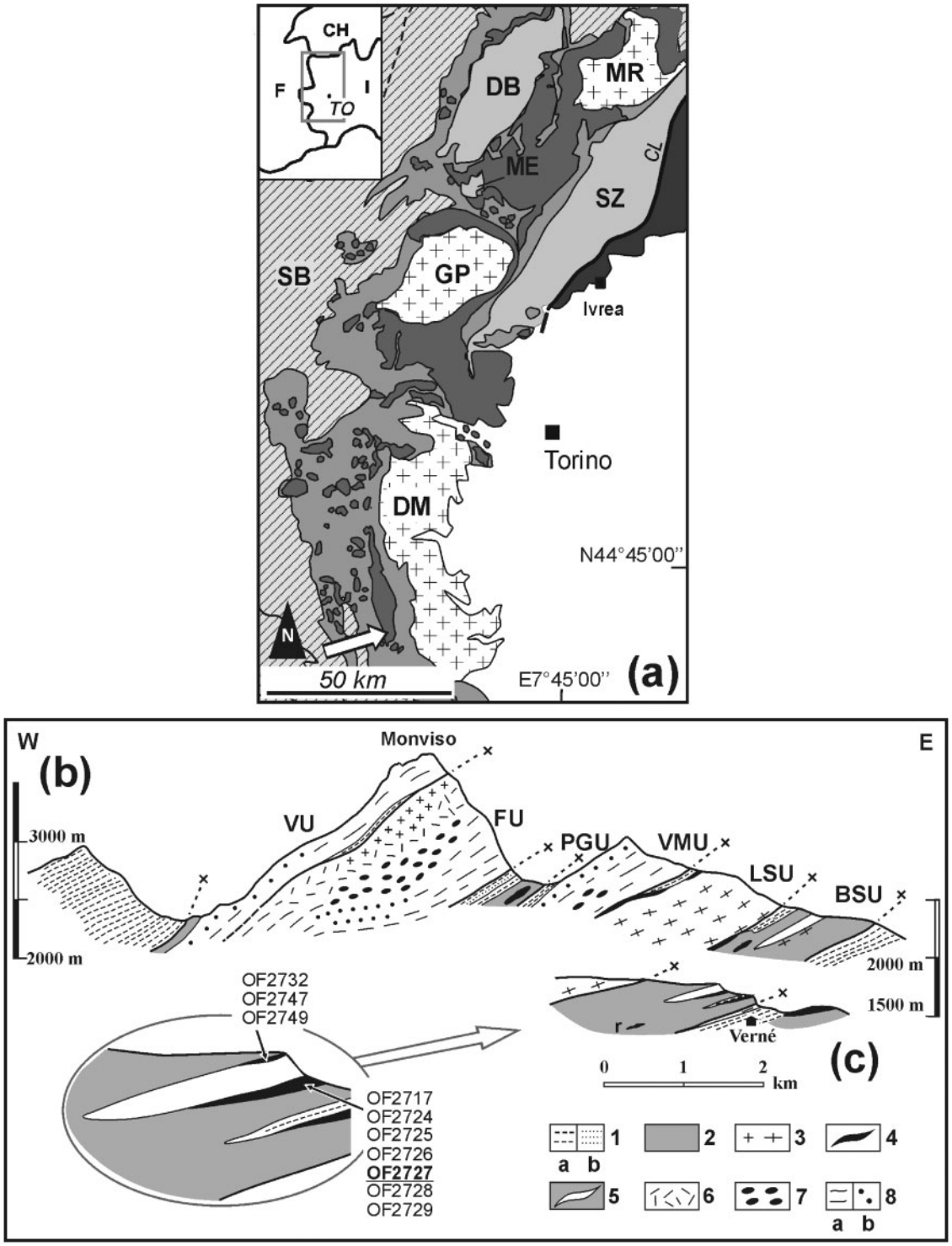

Fig. 1. (a) Simplified tectonic sketch-map of the Western Alps showing the location of the study area (white arrow) within the Monviso meta-ophiolite. SB, Grand St. Bernard Zone; MR, Monte Rosa; GP, Gran Paradiso; DM, Dora–Maira; DB, Dent Blanche nappe; ME, Monte Emilius nappe; SZ, Sesia–Lanzo Zone; CL, Canavese line. The Calcschists and meta-ophiolites of the Piemonte Zone are shown in medium and dark grey, respectively. (b, c) Schematic cross-sections through the Monviso meta-ophiolite in the upper Po Valley (b) and along the northern side of middle Val Varaita (c). Symbols: 1a, carbonate micaschists; 1b, quartz-rich micaschists and metacherts; 2, serpentinites and antigorite schists; 3, isotropic and foliated metagabbros; 4, FeTi-oxide metagabbros and eclogites (including rodingitized varieties: r); 5, metaplagiogranites; 6, massive metabasalts; 7, pillowed metabasalts; 8a, banded metabasites; 8b, metabasites with breccia texture. VU, Vallanta Unit; FU, Forciolline Unit; PGU, Passo Gallarino Unit; VMU, Viso Mozzo Unit; LSU, Lago Superiore Unit; BSU, Basal Serpentinite Unit. The inset refers to the BSU of Val Varaita and locates the studied FeTi-oxide metagabbro OF2727 and the other FeTi-oxide metagabbro samples from the same area (modified after Castelli & Lombardo, 2007).

(Lombardo *et al.*, 2002; Rubatto & Hermann, 2003) during opening of the Mesozoic Western Alpine Tethys and that underwent eclogite-facies metamorphism during the Eocene Alpine subduction (45 ± 1 Ma; Rubatto & Hermann, 2003). It consists of two types of units: (1) magma-rich units, in which a relatively thick basaltic layer caps gabbros and serpentinized peridotites (Vallanta, Forciolline, Viso Mozzo and Lago Superiore Units); (2) magma-poor units in which serpentinized peridotites are directly covered by a thin sedimentary sequence (Passo Gallarino and Basal Serpentinite Units) (Fig. 1b and c; Lombardo *et al.*, 1978; Lagabrielle & Lemoine, 1997; Castelli & Lombardo, 2007, and references therein).

Previous petrological studies of the Monviso meta-ophiolite units were mainly dedicated to estimating the peak P–T conditions experienced during subduction. P–T estimates were obtained for FeTi-oxide metagabbros, MgAl metagabbros, metabasalts and metaplagiogranites occurring at various structural positions, using a range of petrological approaches: conventional thermobarometry (Grt–Cpx and Grt–Phe thermometers, Jd-in-omphacite and Si-in-Phe barometers), P–T grids and average P–T methods of Thermocalc (Blake *et al.*, 1995; Messiga *et al.*, 1999; Schwartz *et al.*, 2000; Castelli *et al.*, 2002). Although all these studies concluded that peak metamorphism occurred under a very low thermal gradient (4–9°C km^{-1}), the estimated peak P–T conditions are not constant among the various units and range from a maximum of 620 ± 50°C, 24 ± 1 kbar (Messiga *et al.*, 1999, Lago Superiore Unit) to a minimum of 450 ± 50°C, 12 ± 3 kbar (Schwartz *et al.*, 2000, Viso Mozzo and Passo Gallarino Units). Blake *et al.* (1995) and Schwartz *et al.* (2000) documented a common exhumation history under blueschist-facies conditions for all the Monviso units. In contrast, the prograde metamorphic evolution of the Monviso meta-ophiolite was never investigated and no lawsonite-bearing relics have been reported so far in any of the Monviso Units.

In the magma-poor, Basal Serpentinite Unit (BSU) of Varaita Valley, a primary plagiogranite–FeTi-oxide gabbro association is exposed (Fig. 1c), which represents an evolved tholeiite magma body within ultramafic oceanic crust at a late fractional crystallization stage (Castelli *et al.*, 2002; Castelli & Lombardo, 2007). As a result of the Alpine tectono-metamorphic reworking, the plagiogranite was extensively recrystallized into fine-grained and massive, jadeite + quartz ± phengite ± garnet ± ferroglaucophane rocks, locally cut by albite + quartz-bearing leucocratic layers that were interpreted as late-magmatic dikes. The FeTi-oxide gabbro, from which the studied sample was collected, was converted into omphacite + garnet + rutile ± glaucophane eclogite, which forms a discontinuous envelope around the metaplagiogranite body or occurs as decimetre-thick folded boudins within the same metaplagiogranite. Preliminary P–T estimates (based on calculated phase compatibilities and phengite geobarometry) indicated $T > 575$°C and $P > 19{\cdot}5$ kbar for the peak Alpine assemblage in the metaplagiogranite body, in agreement with garnet–clinopyroxene geothermometry from the associated FeTi-oxide metagabbro samples, which yielded $T = 545 \pm 35$°C at $P = 20$ kbar (Castelli *et al.*, 2002).

Mineral assemblages and bulk-rock compositions of the BSU metaplagiogranite–FeTi-oxide metagabbro association were given by Castelli & Lombardo (2007). The FeTi-oxide metagabbro samples (see inset in Fig. 1c for their location) are characterized by very similar microstructures (compare Fig. SM1, available as Supplementary Material at http://www.petrology.oxfordjournals.org/), mineral assemblages and bulk-rock compositions (Castelli & Lombardo, 2007). A detailed petrographic re-investigation of all the FeTi-oxide metagabbros (10 samples from the same area) allowed us to recognize, for the first time in the Monviso meta-ophiolite, the occurrence of lawsonite relics in both garnet and omphacite cores of the OF2727 metagabbro sample.

PETROGRAPHY AND MINERAL CHEMISTRY

The FeTi-oxide metagabbro OF2727 is a fine-grained rock with an exceptionally preserved high-pressure mineral assemblage. It consists of omphacite, garnet and rutile with minor blue amphibole and very minor lawsonite, talc and jadeite (Fig. 2; Fig. SM1 and SM2, Supplementary Material). Microstructural relics of the magmatic assemblage are represented by a few millimetre-sized clinopyroxene porphyroclasts, completely re-equilibrated as omphacite during the high-pressure metamorphic event, and by rutile aggregates grown at the expense of interstitial magmatic ilmenite. The omphacite and rutile aggregates are slightly oriented to define a weak foliation. Representative analyses of garnet, clinopyroxene, amphibole, talc, lawsonite and chlorite are given in Tables 1 and 2; analytical methods are described in Appendix A. Mineral abbreviations are from Bucher & Frey (2002).

Both garnet and omphacite are strongly zoned (Figs 2b–d and 3; Fig. SM3a and b, Supplementary Material). Garnet occurs as small idioblasts (up to 0·5 mm in diameter) with reddish cores (Grt_1) crowded with small inclusions of omphacite and minor lawsonite (Fig. 2e), glaucophane and chlorite, and a pinkish rim (Grt_2) with minor, but larger, inclusions of omphacite and very minor talc. The textural zoning of garnet corresponds to a sharp chemical zoning. Mn shows a bell-shaped pattern typical of prograde zoning (X_{Mn} is 0·24 to 0·00 from core to rim), balanced by an increase in both X_{Mg} and X_{Fe} (X_{Mg} is 0·01 to 0·12, and X_{Fe} is 0·56 to 0·82 from core to rim,

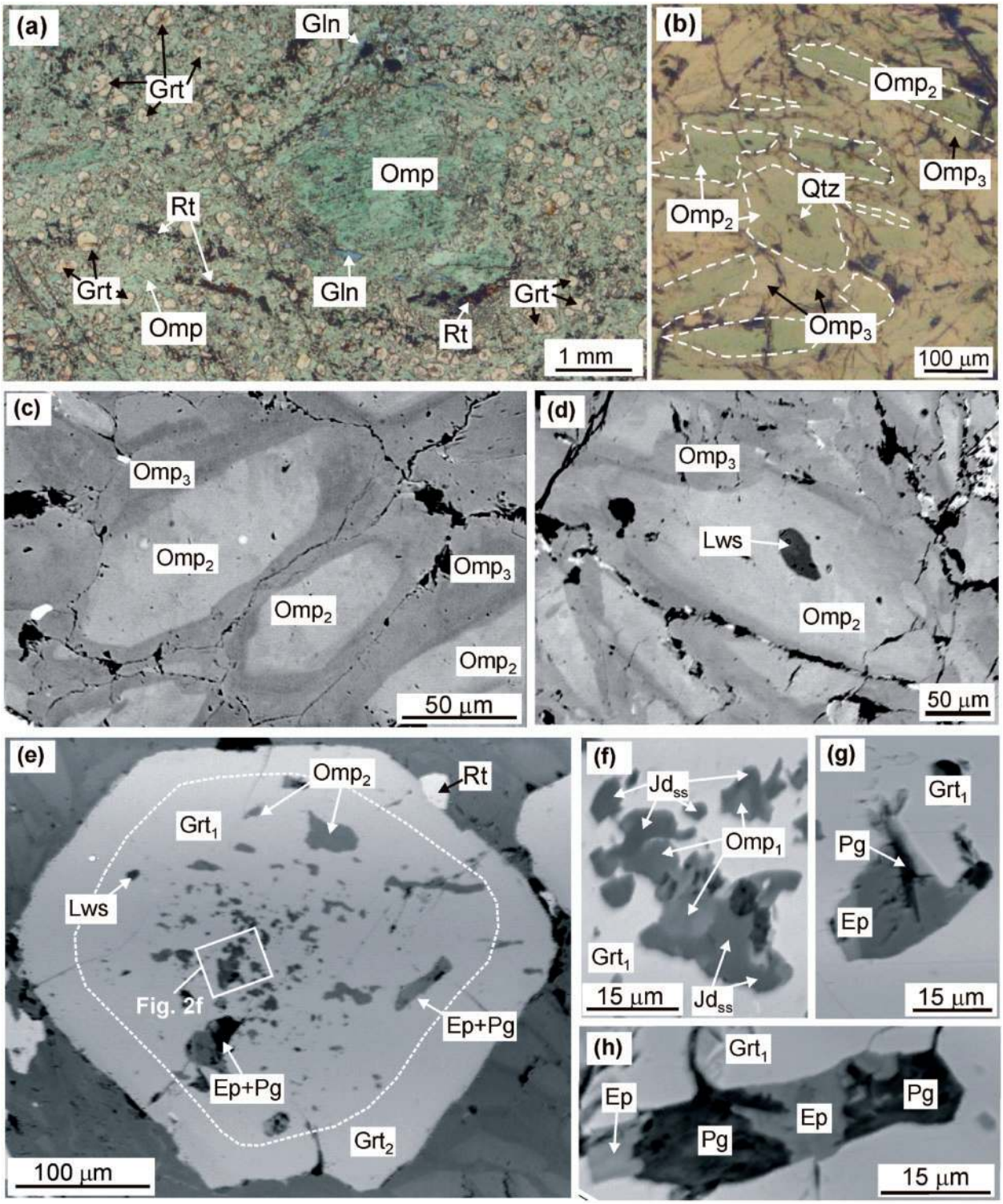

Fig. 2. Representative microstructures of the eclogite-facies FeTi-oxide metagabbro. (a) Large igneous clinopyroxene porphyroclast, completely re-equilibrated as omphacite, set in a matrix consisting of omphacite, garnet and rutile. Rare glaucophane crystals are scattered in the matrix. Plane-polarized light (PPL). Mineral abbreviations according to Bucher & Frey (2002). (b) Detail of the strongly zoned matrix omphacite, showing a dark green core (Omp_2, contoured by dashed line) and a light green rim (Omp_3). PPL. (c) Back-scattered electron image (BSE) of the zoned omphacite crystals. The lighter core (Omp_2) is richer in the aegirine component compared with the darker rim (Omp_3). (d) BSE image of relic lawsonite preserved as an inclusion in the core of matrix omphacite. (e) BSE image of a zoned garnet crystal with the core (Grt_1) crowded with inclusions. [Note lawsonite inclusions (and the epidote + paragonite pseudomorphs after lawsonite) occurring only in Grt_1.] (f) Detail of the fine-grained inclusions occurring in the inner core of garnet in (e). Jd_{ss} and Omp_1 are darker and lighter grey, respectively. BSE image. (g, h) BSE images of epidote + paragonite pseudomorphs after lawsonite, included in Grt_1.

Table 1: Representative EMPA-WDS(*) and SEM-EDS analyses of garnet and clinopyroxene

	Garnet									Clinopyroxenes									
	Grt_1					Grt_2				Jd_{ss}		Omp_1		Omp_2			Omp_3		
Site:	(1a)	(1b)	(1c)	(1d)	(1e)	(2a)	(2b)	(2c)	Site:	in Grt_1		in Grt_1		core	core	in Grt_1	rim	rim	in Grt_2
Analysis:	m11-17*	m11-19*	m11-21*	m11-25*	m11-25*	m11-25*	m11-28*	m11-30*	Analysis:	20-2	5-29	1-29	11-4	m_om 21*	m_om 20*	m_om 17*	m_om 19*	m_om 25*	9-35
SiO_2	36·68	37·06	37·03	37·17	37·11	36·96	36·82	37·18	SiO_2	57·37	57·18	53·75	53·90	55·50	55·75	55·51	56·17	56·06	55·73
Al_2O_3	19·86	20·16	20·27	20·21	20·54	20·34	20·52	20·87	Al_2O_3	17·32	16·24	5·79	6·28	7·18	7·56	6·13	8·96	8·77	9·43
Fe_2O_3	3·06	2·70	1·50	1·21	0·31	0·25	0·55	0·68	Fe_2O_3	—	—	—	—	—	—	—	—	—	—
FeO	24·50	25·51	28·14	30·27	33·72	35·64	35·62	34·68	FeO_{tot}	6·69	6·45	15·89	14·70	13·30	12·78	14·33	8·85	8·49	8·07
MnO	8·51	5·29	3·91	2·70	1·30	0·42	0·16	1·11	MnO	b.d.l.	b.d.l.	b.d.l.	b.d.l.	b.d.l.	0·03	0·03	b.d.l.	0·04	b.d.l.
MgO	0·33	0·60	0·72	0·86	0·96	1·46	1·54	1·96	MgO	2·45	3·22	5·30	5·79	5·33	5·19	5·79	6·56	6·55	6·90
CaO	7·13	8·78	8·41	7·73	6·05	4·69	4·31	3·86	CaO	4·29	4·83	10·72	9·84	8·93	8·87	10·12	10·77	10·67	11·19
Na_2O	b.d.l.	b.d.l.	b.d.l.	b.d.l.	b.d.l.	b.d.l.	b.d.l.	b.d.l.	Na_2O	12·32	11·92	7·89	8·45	9·44	9·36	8·59	8·43	8·39	8·32
Total	100·07	100·11	99·99	100·14	100·00	99·75	99·52	100·35	Total	101·01	100·42	100·60	100·31	99·68	100·76	100·50	99·74	98·97	100·44
Equiv. O	12	12	12	12	12	12	12	12		6	6	6	6	6	6	6	6	6	6
Si	2·98	2·99	2·99	3·00	3·01	3·01	3·00	2·99	Si	1·99	1·99	1·98	1·98	2·00	2·01	2·00	2·01	2·02	1·99
Al	1·90	1·91	1·93	1·92	1·96	1·95	1·97	1·98	Al	0·71	0·67	0·25	0·27	0·31	0·32	0·26	0·38	0·37	0·40
Fe^{3+}	0·19	0·16	0·09	0·07	0·02	0·02	0·03	0·04	Fe^{3+}	0·15	0·15	0·35	0·38	0·35	0·31	0·35	0·19	0·17	0·17
Fe^{2+}	1·66	1·72	1·90	2·04	2·28	2·42	2·42	2·33	Fe^{2+}	0·05	0·04	0·14	0·07	0·05	0·08	0·09	0·08	0·08	0·06
Mn	0·59	0·36	0·27	0·18	0·09	0·03	0·01	0·08	Mn	0·00	0·00	0·00	0·00	0·00	0·00	0·00	0·00	0·00	0·00
Mg	0·04	0·07	0·09	0·10	0·12	0·18	0·19	0·24	Mg	0·13	0·17	0·29	0·32	0·29	0·28	0·31	0·35	0·35	0·37
Ca	0·62	0·76	0·73	0·67	0·52	0·41	0·38	0·33	Ca	0·16	0·18	0·42	0·39	0·35	0·34	0·39	0·41	0·41	0·43
Na	0·00	0·00	0·00	0·00	0·00	0·00	0·00	0·00	Na	0·83	0·81	0·56	0·60	0·66	0·66	0·60	0·58	0·59	0·58
X_{Mg}	0·01	0·02	0·03	0·03	0·04	0·06	0·06	0·08	X_{Aeg}	0·14	0·15	0·34	0·36	0·35	0·32	0·34	0·19	0·17	0·20
X_{Fe}	0·57	0·59	0·64	0·68	0·76	0·80	0·81	0·78	X_{Jd}	0·69	0·65	0·24	0·26	0·31	0·31	0·26	0·38	0·37	0·39
X_{Ca}	0·21	0·26	0·24	0·22	0·17	0·13	0·13	0·11	$X_{Mg}(Fe_{tot})$	0·40	0·47	0·37	0·41	0·42	0·42	0·41	0·57	0·58	0·61
X_{Mn}	0·20	0·12	0·09	0·06	0·03	0·01	0·00	0·03	$Fe^{3+}/\Sigma Fe$	0·76	0·81	0·72	0·84	0·87	0·79	0·80	0·70	0·67	0·74
$Fe^{3+}/\Sigma Fe$	0·10	0·09	0·05	0·03	0·01	0·01	0·01	0·02											

b.d.l., below detection limit. Details on the $Fe^{3+}/\Sigma Fe$ calculation in both garnet and clinopyroxene are given in Appendix A.

Table 2: Representative SEM-EDS analyses of glaucophane, talc, lawsonite and chlorite

	Glaucophane				Talc		Lawsonite			Chlorite
	Gln_1	Gln_2								
Site:	In Grt_1	Matrix			In Omp_3		In Grt_1	In Omp_2		In Grt_1
Analysis:	9-3	6-1	10-4		10-3		20-13	8-5		11-7
SiO_2	57·34	57·06	57·95	SiO_2	60·48	SiO_2	37·43	37·15	SiO_2	25·39
Al_2O_3	7·87	9·34	9·58	Al_2O_3	b.d.l.	Al_2O_3	30·39	29·79	Al_2O_3	40·69
FeO_{tot}	13·36	14·27	13·10	FeO_{tot}	9·00	FeO_{tot}	1·98	1·48	FeO_{tot}	25·09
MnO	b.d.l.	b.d.l.	b.d.l.	MnO	b.d.l.	MnO	b.d.l.	b.d.l.	MnO	b.d.l.
MgO	10·45	8·76	9·71	MgO	25·09	MgO	b.d.l.	b.d.l.	MgO	3·12
CaO	0·76	0·68	0·55	CaO	b.d.l.	CaO	17·32	17·63	CaO	b.d.l.
Na_2O	6·75	7·05	6·84	Na_2O	b.d.l.	Na_2O	b.d.l.	b.d.l.	Na_2O	b.d.l.
Total	97·21	97·57	98·29	Total	99·08	Total	87·33	86·21	Total	94·29
Equiv. O	23	23	23		14		8	8		14
Si	7·98	7·97	7·96	Si	4·02	Si	2·00	2·01	Si	2·40
Al	1·29	1·54	1·55	Al	0·00	Al	1·92	1·90	Al	4·53
Fe^{3+}*	0·69	0·40	0·55	Fe^{3+}*	0·00	Fe^{3+}*	0·08	0·07	Fe^{3+}*	0·00
Fe^{2+}	0·86	1·26	0·95	Fe^{2+}	0·50	Fe^{2+}	0·01	0·00	Fe^{2+}	1·98
Mn	0·00	0·00	0·00	Mn	0·00	Mn	0·00	0·00	Mn	0·00
Mg	2·17	1·82	1·99	Mg	2·48	Mg	0·00	0·00	Mg	0·44
Ca	0·11	0·10	0·08	Ca	0·00	Ca	0·99	1·02	Ca	0·00
Na	1·82	1·91	1·82	Na	0·00	Na	0·00	0·00	Na	0·00
Sum	14·94	15·01	14·90	Sum	7·00	Sum	5·00	5·00	Sum	9·34
$X_{Mg}(Fe_{tot})$	0·58	0·52	0·57	X_{Fe}	0·17				$X_{Mg}(Fe_{tot})$	0·18
Al(IV)	0·02	0·03	0·04							
Al(VI)	1·28	1·51	1·51							
Na(M4)	1·82	1·90	1·82							
Na(A)	0·00	0·01	0·00							

b.d.l., below detection limit.
*Fe^{3+} estimated by stoichiometry (for glaucophane on the basis of 23 oxygens and 15 cations excluding Ca and Na).

respectively). Fe^{3+} shows the same bell-shaped trend as Mn, reaching the maximum values in the core ($Fe^{3+}/\Sigma Fe = 0{\cdot}11$) and progressively decreasing towards the rim ($Fe^{3+}/\Sigma Fe = 0{\cdot}00$). Ca zoning is more complex, slightly increasing from the inner core to the outer core and decreasing toward the rim (X_{Ca} varies from 0·21 to 0·27 and to 0·11) (Fig. 3; Fig. SM4, available as Supplementary Material) [$X_{Mn} = Mn/(Ca + Mg + Fe^{2+} + Mn)$; $X_{Mg} = Mg/(Ca + Mg + Fe^{2+} + Mn)$; $X_{Ca} = Ca/(Ca + Mg + Fe^{2+} + Mn)$; $X_{Fe} = Fe^{2+}/(Ca + Mg + Fe^{2+} + Mn)$; $Fe^{3+}/\Sigma Fe = Fe^{3+}/(Fe^{3+} + Fe^{2+})$]. The transition from the reddish core (Grt_1) to the pinkish rim (Grt_2) is marked by an abrupt decrease in X_{Ca} balanced by an increase in X_{Mg}. Locally, a slight increase in X_{Mn} suggests that partial resorption occurred at the garnet rim (Fig. 3).

Four Na-clinopyroxene types, occurring in different microstructural sites, have been recognized. Omp_1 consists of rare inclusions in the inner garnet core, with $X_{Aeg} = 0{\cdot}29$–$0{\cdot}37$, $X_{Jd} = 0{\cdot}22$–$0{\cdot}26$ and $X_{Mg}(Fe_{tot}) = 0{\cdot}36$–$0{\cdot}44$. A more jadeitic pyroxene ($X_{Aeg} = 0{\cdot}09$–$0{\cdot}24$; $X_{Jd} = 0{\cdot}58$–$0{\cdot}69$, subsequently referred to as Jd_{ss}) occurs in the same microstructural position as Omp_1; although Jd_{ss} and Omp_1 rarely show equilibrium contacts (Fig. 2f), their occurrence in the inner garnet cores would suggest they were coexisting clinopyroxenes. Omp_2 occurs both in the deep green core of matrix nematoblasts (Fig. 2b) and as inclusions in garnet cores (Grt_1) (Fig. 2e), whereas Omp_3 forms the light green rim of the matrix nematoblasts (Fig. 2b) and it is locally included in garnet rim (Grt_2) (Fig. 3). Omp_2 has higher X_{Aeg} and lower X_{Jd} and X_{Mg}

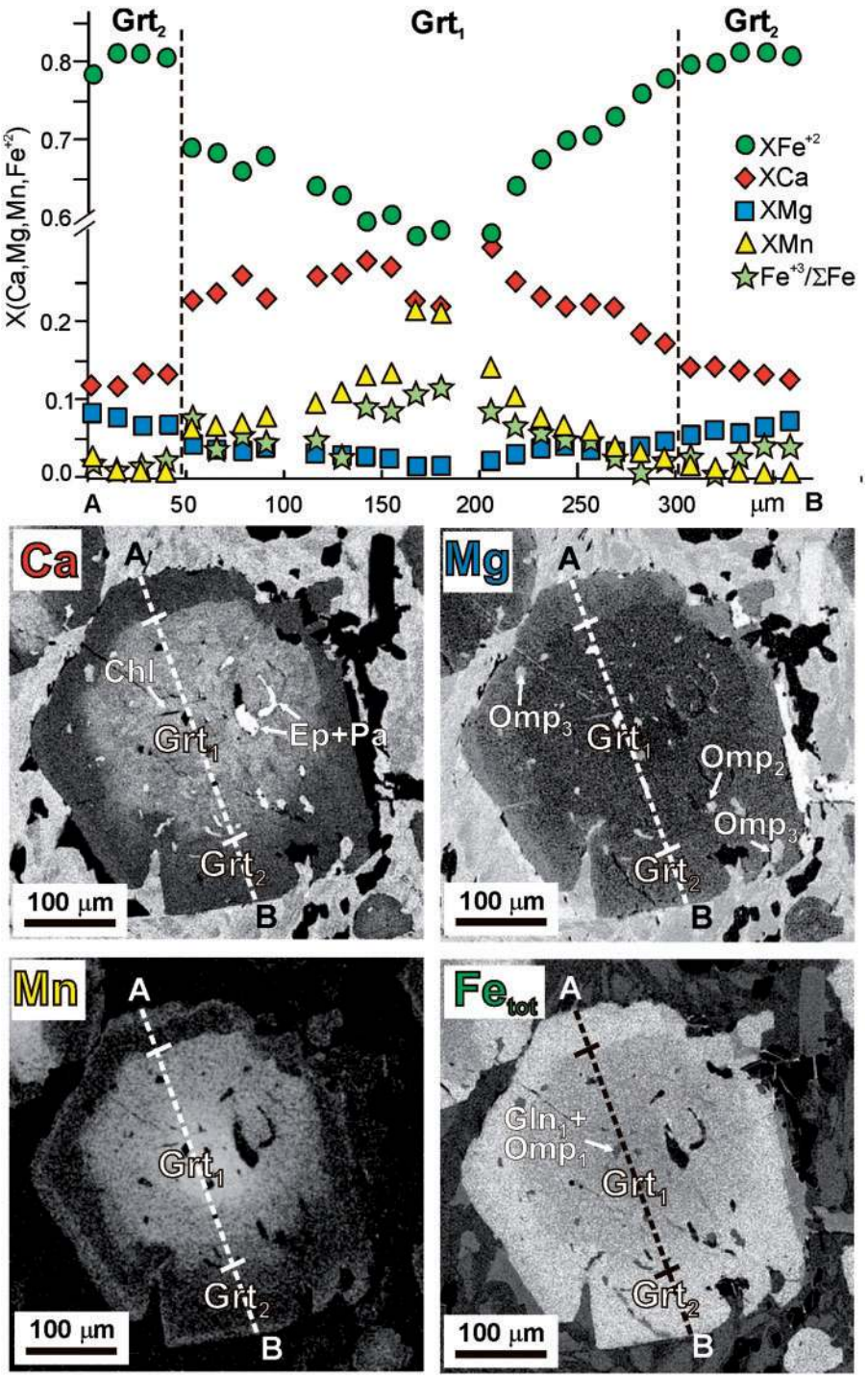

Fig. 3. Compositional profile and Ca, Mg, Mn and Fe_{tot} X-ray maps of a representative garnet crystal (see also Fig. SM3 in the Supplementary Material). In each map, lighter grey implies higher concentration, as shown by quantitative spot analyses. The dashed line in the X-ray maps locates the compositional profile.

[$X_{Aeg} = 0{\cdot}35$-$0{\cdot}28$; $X_{Jd} = 0{\cdot}25$-$0{\cdot}35$; $X_{Mg}(Fe_{tot}) = 0{\cdot}40$–$0{\cdot}50$; aegirine–augite according to the classification of Morimoto *et al.* (1988)] than Omp_3 [$X_{Aeg} = 0{\cdot}24$-$0{\cdot}14$; $X_{Jd} = 0{\cdot}35$-$0{\cdot}45$; $X_{Mg}(Fe_{tot}) = 0{\cdot}52$–$0{\cdot}66$] (Fig. 4 and Tables 1 and 3) [$X_{Aeg} = Fe^{3+}/(Fe^{3+} + Al^{VI} + Fe^{2+} + Mg)$; $X_{Jd} = Al/(Fe^{3+} + Al^{VI} + Fe^{2+} + Mg)$; $X_{Mg}(Fe_{tot}) = Mg/(Mg + Fe)$]. The large clinopyroxene porphyroclasts, interpreted as microstructural relics of the magmatic

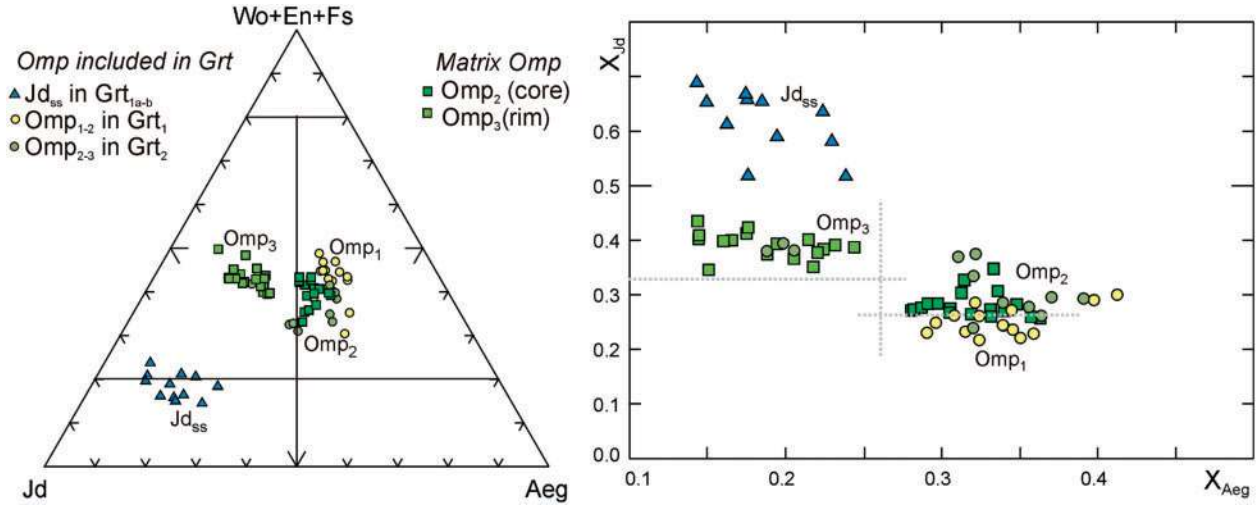

Fig. 4. Compositions of omphacites plotted in the Morimoto *et al.* (1988) diagram and in the X_{Aeg} vs X_{Jd} diagram. $X_{Aeg} = Fe^{3+}/(Fe^{3+} + Al^{VI} + Fe^{2+} + Mg)$; $X_{Jd} = Al/(Fe^{3+} + Al^{VI} + Fe^{2+} + Mg)$.

assemblage, are patchly zoned omphacites, compositionally similar to either Omp_2 or Omp_3.

Blue amphibole (glaucophane according to the Na-amphibole classification of Leake *et al.*, 1997) is a minor phase occurring in two microstructures: (1) as rare prograde inclusions (Gln_1) occurring in the inner core of garnet, with $X_{Mg}(Fe_{tot}) = 0{\cdot}52–0{\cdot}58$; (2) as a retrograde glaucophane occurring as small idioblasts (Gln_2) statically overgrowing the weakly-oriented omphacite and rutile of the matrix (Fig. 2a) and showing the same composition as Gln_1.

Lawsonite is rare and mainly preserved as small inclusions in both garnet (Grt_1) and omphacite (Omp_2) cores (Figs 2d and e). Larger lawsonite inclusions in garnet and omphacite are generally replaced by fine-grained aggregates of epidote ($Zo_{70–87}$) and paragonite (Figs 2e, g, h and 3). Lawsonite has not been observed in the matrix, either as preserved crystals or as its pseudomorphic replacements. Rare talc ($X_{Fe} = 0{\cdot}15–0{\cdot}19$) is included both in the garnet rim (Grt_2) and in the omphacite porphyroclasts. Very rare chlorite flakes have been observed in the inner garnet cores (Grt_1) (Fig. 3) and interpreted as preserved relics of a prograde assemblage. Finally, rare quartz has been observed as inclusions in both omphacite and garnet (Fig. 2b).

Despite the relatively simple paragenesis, garnet and omphacite zoning together with the distribution of inclusions in garnet and omphacite allow us to define a prograde metamorphic evolution, which is summarized in Table 3. Two pyroxenes ($Jd_{ss} + Omp_1$) were stable at relatively low T, before and at the onset of garnet growth. Coexisting jadeitic pyroxene + omphacite pairs in natural assemblages are rare (e.g. Matsumoto & Hirajima, 2005; Tsujimori *et al.*, 2005, 2006*a*, 2006*b*; Miyazoe *et al.*, 2009) and are often due to the presence of a T-dependent miscibility gap approximately located at $Jd_{60–85}$ (e.g. Green *et al.*, 2007). Compositions of Omp_1 ($Jd_{22–26}$) and Jd_{ss} ($Jd_{58–69}$) in sample OF2727 lie outside this generally accepted miscibility gap. Alternatively, these compositions could be due to 'mosaic equilibrium' phenomena (i.e. Jd-rich and Jd-poor clinopyroxenes grew in former plagioclase and pyroxene microdomains, respectively) (e.g. Korzhinskii, 1959). Garnet cores (Grt_1) then grew in equilibrium with a single omphacitic clinopyroxene (Omp_2), lawsonite and rutile, whereas the growth of garnet rims (Grt_2) coincides with (1) a change in the omphacite composition (Omp_3), (2) the disappearance of lawsonite and (3) the development of talc. Na-amphibole (Gln_2) is a later phase, statically overgrowing the prograde and peak parageneses.

PSEUDOSECTION MODELLING

Pseudosection modelling is currently recognized as one of the most powerful methods by which to gain thermobarometric information on rocks, because it provides a framework to interpret both textural information and mineral compositions in terms of P–T evolution (e.g. Powell & Holland, 2008). The mafic system has been widely investigated since the late 1990s (e.g. Clarke *et al.*, 1997, 2006; Will *et al.*, 1998; Carson *et al.*, 1999; Štípská & Powell, 2005; Davis & Whitney, 2006, 2008; Groppo *et al.*, 2007, 2009*a*) but until a few years ago modelling of Fe^{3+}-bearing systems was hampered by the lack of solid-solution models for Fe^{3+}-bearing mineral end-members (Will *et al.*, 1998; Wei *et al.*, 2003). Following the pioneering work of Warren & Waters (2006) on Fe^{3+}-bearing eclogites and blueschists from Oman, and thanks to recent improvements in the

Table 3: Metamorphic evolution

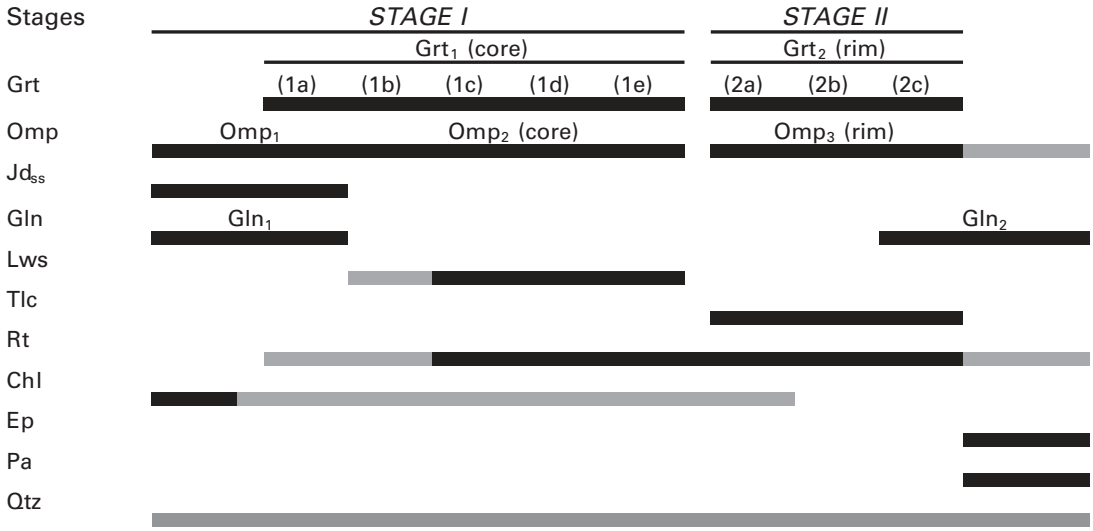

Grey lines represent phases presumed to be stable on the basis of microstructural observations.

Compositional range of Grt and Omp during stages I and II

		STAGE I					STAGE II		
		Grt_1 (core)					Grt_2 (rim)		
Grt (×100)		(1a)	(1b)	(1c)	(1d)	(1e)	(2 a)	(2b)	(2c)
X_{Ca}		21–24	22–27	25–21	22–18	20–17	15–13	14–12	11–13
X_{Mg}		1–2	2–3	2–4	3–4	3–5	5–6	6–9	10–12
$X(Fe^{2+})$		56–62	58–63	65–70	70–73	69–77	77–82	79–81	74–80
X_{Mn}		24–15	14–8	8–6	6–4	4–3	3–1	1–0	0–2
$Fe^{3+}/\Sigma Fe$		11–8	9–5	6–4	4–2	4–2	0–2	0–4	0–2
Omp (×100)	Omp_1	Omp_2					Omp_3		
X_{Aeg}	29–37	35–28					24–14		
X_{Jd}	22–26	25–35					35–45		
X_{Mg}	36–44	40–50					52–66		

solution models for omphacite (Green *et al.*, 2007) and amphibole (Diener *et al.* 2007), oxidized systems have begun to be successfully investigated (e.g. Groppo *et al.*, 2009*b*; Wei *et al.*, 2009). We have therefore used this approach; details of the pseudosection calculations are given in Appendix B.

Bulk-rock composition

The bulk-rock composition of sample OF2727 has been estimated by two methods: (1) average of 15 scanning electron microscope–energy-dispersive spectrometry (SEM-EDS) analyses of 4·70 mm × 3·20 mm selected areas within a polished thin section; (2) combining mineral modes and compositions (see Appendix A, and Table SM1 and Fig. SM2 in Supplementary Material, for details). These compositions have been compared with the inductively coupled plasma–mass spectrometry (ICP-MS) analysis of the same sample (Castelli & Lombardo 2007, table 2). Bulk compositions obtained with methods (1) and (2) are very similar and both slightly differ from the ICP-MS analysis in their lower CaO and Al_2O_3 contents (Table 4, and Fig. SM4 in Supplementary Material). These small differences may account for the presence of rare epidote-bearing domains in the hand specimen crushed for ICP-MS analysis, by analogy with those observed in other samples collected from the same area. We have therefore used the bulk composition obtained from method (1) because of its statistical significance and the better microstructural control. Bulk compositions of other FeTi-oxide metagabbros from the Western Alps (Monviso meta-ophiolites: Castelli & Lombardo, 2007; Lanzo and Rocciavrè massifs: Pognante *et al.*, 1982;

Table 4: Effective bulk compositions used for calculation of pseudosections (mol %)

	OF2727										OF2717	OF2732
Stage:	Stage I					Stage II						
	1a*	1b	1c	1d	1e	2a	2b	2c	MM&C†	C&L(07)**	C&L(07)**	C&L(07)**
SiO_2	49·51	49·78	50·03	50·38	50·66	51·20	52·29	52·75	50·01	49·42	53·63	55·40
TiO_2	4·57	4·60	4·62	4·66	4·68	4·73	4·83	4·87	7·02	4·07	2·75	3·39
Al_2O_3	6·68	6·72	6·76	6·81	6·85	6·92	7·03	7·13	7·64	9·05	8·42	7·76
FeO	13·06	12·82	12·66	12·30	12·06	12·08	10·87	10·33	11·79	9·21	13·31	11·44
Fe_2O_3	3·25	3·20	3·15	3·06	3·01	2·21	1·99	1·88	2·39	3·15	1·79	2·92
MnO	0·24	0·14	0·10	0·06	0·05	0·02	0·01	0·00	0·31	0·24	0·29	0·24
MgO	7·96	8·00	8·03	8·06	8·10	8·17	8·25	8·28	6·65	8·00	8·38	6·77
CaO	9·07	9·00	8·93	8·90	8·81	8·81	8·74	8·72	8·83	10·82	6·81	7·66
Na_2O	5·66	5·74	5·73	5·78	5·80	5·86	5·99	6·04	5·36	6·03	4·63	4·42
Total	100·00	100·00	100·00	100·00	100·00	100·00	100·00	100·00	100·00	100·00	100·00	100·00
$X(Fe_2O_3)$	0·20	0·20	0·20	0·20	0·20	0·15	0·15	0·15	0·17	0·25	0·12	0·20

*Starting bulk-composition of sample OF2727 obtained from SEM-EDS areal analyses (see text for the Fe_2O_3 vs FeO calculation).
†Bulk-composition of sample OF2727 obtained by combining Mineral Modes and Compositions (see Appendix A for details).
‡ICP-MS and wet chemical data from Castelli & Lombardo (2007), converted into mol % and normalized to 100. Compositions of two other FeTi-oxide metagabbro samples are shown for comparison.

Pognante & Toscani, 1985; Aosta Valley: Bocchio *et al.*, 2000) are reported for a comparison in Table 4, and Fig. SM4 in the Supplementary Material.

Fractionation effects on the bulk-rock compositions

The occurrence of strongly zoned garnet porphyroblasts probably caused chemical fractionation of the bulk-rock composition, as a result of the preferential sequestration of some elements in the garnet cores. In this case a single pseudosection, calculated on the base of the bulk-rock composition, is inadequate to model the entire evolution of the rock: modelling separate pseudosections using the effective composition representative of each equilibration volume will result in a much more accurate reconstruction of the P–T path. Several methods have been proposed to calculate the effective bulk composition modified because of elemental partitioning related to garnet growth (Stüwe, 1997; Marmo *et al.*, 2002; Evans, 2004; Zuluaga *et al.*, 2005; Gaidies *et al.*, 2006; Groppo & Rolfo, 2008; Groppo *et al.*, 2009*a*). For the studied sample, bulk compositions effectively reacting during each stage of garnet growth have been calculated following the method described by Evans (2004) and Gaidies *et al.* (2006). This method applies a Rayleigh fractionation model based on the measured Mn content of garnet and requires that a strong correlation between the concentration of Mn vs Fe, Mg and Ca in garnet exists. To model the bulk-composition fractionation as a continuous process, several growth increments should be considered for garnet (in other words, the more growth increments used, the more detailed will be the modelling of fractionation effects). For this reason, garnet zoning has been divided into eight growth shells on the basis of the Mn content and the core vs rim size (Fig. SM5a, Supplementary Material). Garnets with the highest and similar MnO contents were selected as representative of garnet crystals sectioned through the actual core. The garnet cores have been divided into five shells (Grt_{1a} to Grt_{1e}), whereas the garnet rims have been divided into three shells (Grt_{2a} to Grt_{2c}). The studied sample shows significant fractionation effects (Fig. SM5, Supplementary Material) and eight bulk compositions have thus been considered (Table 4), representative of equilibrium compositions during the growth of Grt_{1a} to Grt_{2c}.

Although omphacite is also zoned, bulk-composition fractionation as a result of its growth has not been considered, mainly because the compositional differences between Omp_2 and Omp_3 are much less pronounced with respect to those between Grt_1 and Grt_2.

Estimation of Fe_2O_3 in the modelled bulk compositions

The bulk $Fe_2O_3/(FeO+Fe_2O_3)$ ratio [subsequently referred to as $X(Fe_2O_3)=Fe_2O_3/(FeO+Fe_2O_3)$ mol %]

appears to change during the metamorphic evolution of the rock, as shown by the different Fe^{3+} contents in the omphacite and garnet cores (Omp_2, Grt_1) and rims (Omp_3, Grt_2), respectively. Omphacite and garnet zoning suggests that $X(Fe_2O_3)$ decreased during the rock evolution; moreover, the abrupt transition from Grt_1 to Grt_2 and from Omp_2 (included in Grt_1) to Omp_3 (included in Grt_2) suggests that the decrease in $X(Fe_2O_3)$ occurred rapidly and discontinuously and coincides with the transition from garnet cores to garnet rims (i.e. stages I to II of Table 3). As a consequence, the $X(Fe_2O_3)$ ratio in the bulk-rock composition cannot be directly measured from the sample, because $X(Fe_2O_3)$ values obtained by conventional bulk-methods (e.g. wet chemical determination) or by combining mineral modes and compositions are not representative of the equilibrium composition at each modelled stage of the metagabbro evolution.

The $X(Fe_2O_3)$ during stages I and II was therefore estimated using a 'best-fit' criterion between modelled isopleths and the measured compositions of garnet and omphacite. In more detail, several P–T pseudosections were calculated using various $X(Fe_2O_3)$ values, ranging from $X(Fe_2O_3) = 0{\cdot}10$ to $X(Fe_2O_3) = 0{\cdot}25$ mol %. For each stage, the $X(Fe_2O_3)$ ratio was considered correct when the modelled compositional isopleths of both garnet and omphacite intersected each other, fitting the measured mineral compositions. Conversely, if the observed mineral assemblages and compositions were not matched by a field in the pseudosection, this indicates that the composition of the equilibration volume was incorrectly assigned (e.g. Powell & Holland, 2008).

Figure SM6a and b (Supplementary Material) shows that for $X(Fe_2O_3) \leq 0{\cdot}15$ and $X(Fe_2O_3) \geq 0{\cdot}25$ mol %, Grt_1 and Omp_2 compositional isopleths do not show any intersection, whereas for $X(Fe_2O_3) = 0{\cdot}20$ mol %, the modelled Grt_1 and Omp_2 compositional isopleths intersect in the omphacite + chlorite + garnet + lawsonite + quartz + rutile field, which is consistent with the inferred prograde assemblage (see Table 3). Therefore, to model the stage I P–T conditions, corresponding to the growth of garnet and omphacite cores (Grt_1 and Omp_2) $X(Fe_2O_3) = 0{\cdot}20$ mol % was used. The stage II P–T conditions, corresponding to the growth of garnet and omphacite rims (Grt_2 and Omp_3), was modelled using a lower $X(Fe_2O_3) = 0{\cdot}15$ mol %, for which the modelled Grt_2 and Omp_3 isopleths intersect (Fig. SM6a).

For comparison, the $X(Fe_2O_3)$ values determined for the whole-rock sample using two techniques—wet chemistry and mineral modes and compositions (see Appendix A for further details)—are reported in Table 4. The wet chemistry method (data from Castelli & Lombardo, 2007) gives an $X(Fe_2O_3)$ slightly higher (0·25 mol %) than that estimated using the 'best-fit' criterion (0·20 and 0·15 mol % for stages I and II, respectively), and this is consistent with the presence of rare epidote-bearing domains in the sample crushed for wet chemistry analysis, as previously suggested. Similar $X(Fe_2O_3)$ values, in the range 0·12–0·26 mol %, have been reported for other FeTi-oxide metagabbros from the Monviso meta-ophiolites (Castelli & Lombardo, 2007; Table 4) and from the Aosta Valley in the Western Alps (Bocchio *et al.*, 2000). Conversely, the $X(Fe_2O_3)$ value measured by combining mineral modes and compositions (0·17 mol %, Table 4) is intermediate between that estimated for stage I and stage II, thus confirming the reliability of the two values here adopted by using the 'best-fit' criterion.

RESULTS

The prograde *P–T* path

Eight pseudosections (1a–1e and 2a–2c for stages I and II, respectively) have been modelled for the studied sample, based on various bulk compositions representing equilibrium compositions during the growth of Grt_{1a} to Grt_{2c} (see Table 4) and, as explained above, at $X(Fe_2O_3) = 0{\cdot}20$ and $X(Fe_2O_3) = 0{\cdot}15$, respectively. Modelled compositional isopleths of garnet (X_{Ca} and X_{Mg}) and omphacite (X_{Aeg}) have been used to constrain the P–T conditions of garnet growth, from stage I ($Grt_{1a–e}$ and Omp_2) to stage II ($Grt_{2a–c}$ and Omp_3). Results are given in Fig. 5, and in Fig. SM7a–d (Supplementary Material), and are summarized in Fig. 6. The estimated modal amounts of each phase and the H_2O wt % are also reported in Table 5. Garnet compositions provide good constraints on temperatures, whereas pressures are better constrained for stage I ($Grt_{1a–e}$) with respect to stage II ($Grt_{2a–c}$) (Figs 5 and 6; Table 5), for which the X_{Ca} and X_{Mg} isopleths of garnet intersect at smaller angles.

Pseudosection modelling shows that the studied eclogite well preserves the metamorphic assemblages that developed along a segment of its subduction path from about 420°C, 16 kbar to 550°C, 25–26 kbar (Fig. 6). The modelled peak temperature must be considered as a minimum, because garnet is partially resorbed at its rim (Fig. 3) and the highest X_{Mg} values may have possibly been reset during retrogression. As a consequence of this P–T trajectory, the eclogite-facies metagabbro passed from the hydrated Grt + Omp + Lws + Chl + Qtz + Rt assemblage (stage I) to the nearly anhydrous Grt + Omp + Tlc + Qtz + Rt assemblage (stage II). In more detail, the transition from stage I to stage II (i.e. from Grt_{1e} to Grt_{2a}) corresponds to an abrupt decrease in the modelled water content in the system ($H_2O = 3{\cdot}5$ to 1·7 wt %; see Table 5 and Fig. 7a), marked by the complete destabilization of lawsonite and chlorite that also accounts for an abrupt increase in density (Table 5, Fig. 7b).

Our pseudosections in the given P–T range do not model two microstructural observations: (1) the coexistence of Omp_1 and Jd_{ss} in the inner garnet core ($Grt_{1a–b}$),

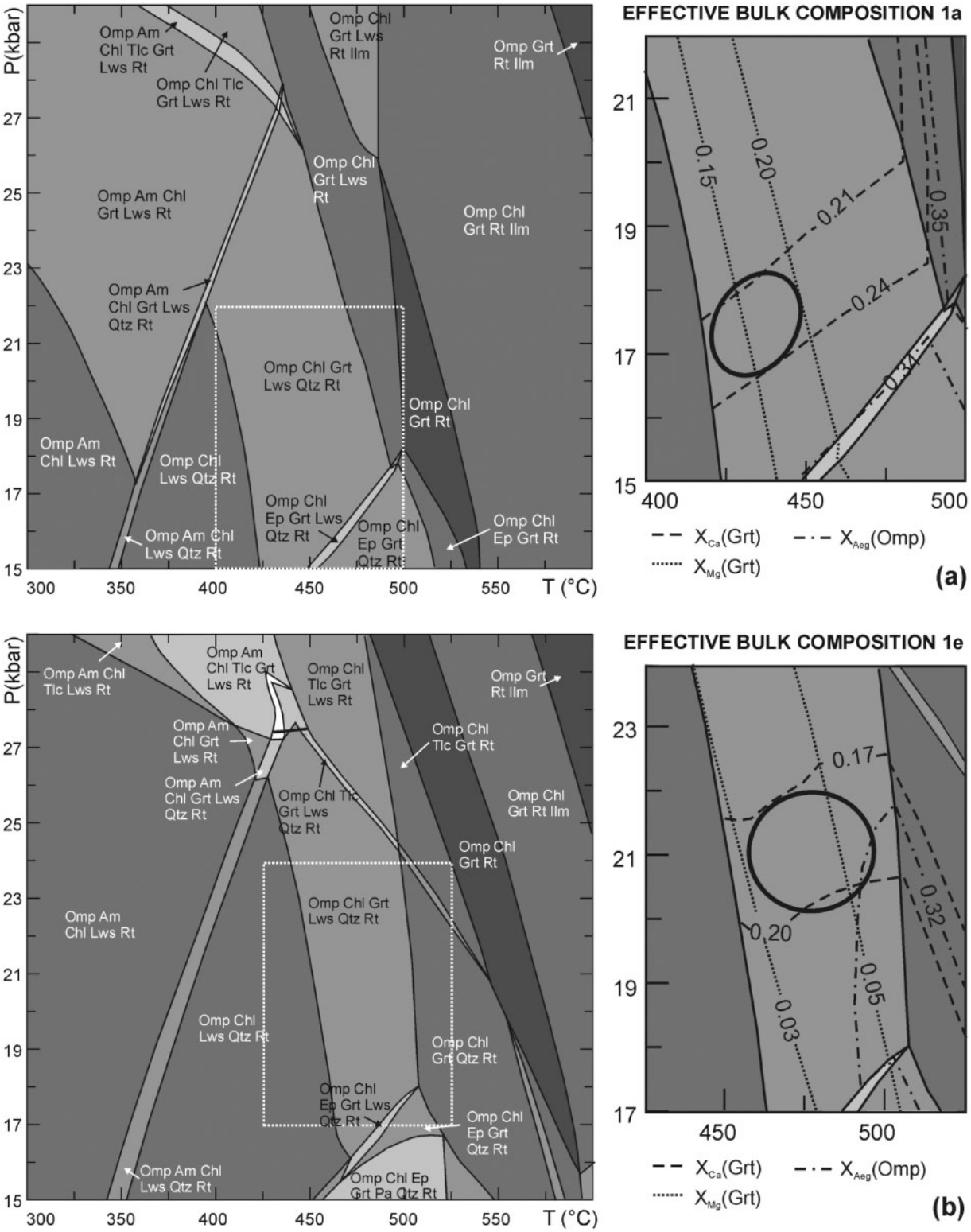

Fig. 5. *P–T* pseudosections for sample OF2727 calculated in the MnNCFMASTHO system at $a(H_2O) = 1$ and $X(Fe_2O_3) = 0{\cdot}20$ (stage I) and $X(Fe_2O_3) = 0{\cdot}15$ (stage II), using the effective bulk compositions calculated for stages la (a), le (b) and 2c (c) (see Table 4). White, light-, medium-, dark- and very dark-grey fields are tri-, quadri-, quini-, esa- and epta-variant fields, respectively. Ellipses in the insets are derived from the intersection of compositional isopleths corresponding to the actual compositions of garnet and constrain the *P–T* conditions of its growth at each of the stages. Thick lines in (b) and (c) are the Qtz–Coe transition. The complete set of pseudosections for stages la–le and 2a–2c with all the compositional isopleths for garnet and omphacite is reported in Fig. SM7a–d, available as Supplementary Material.

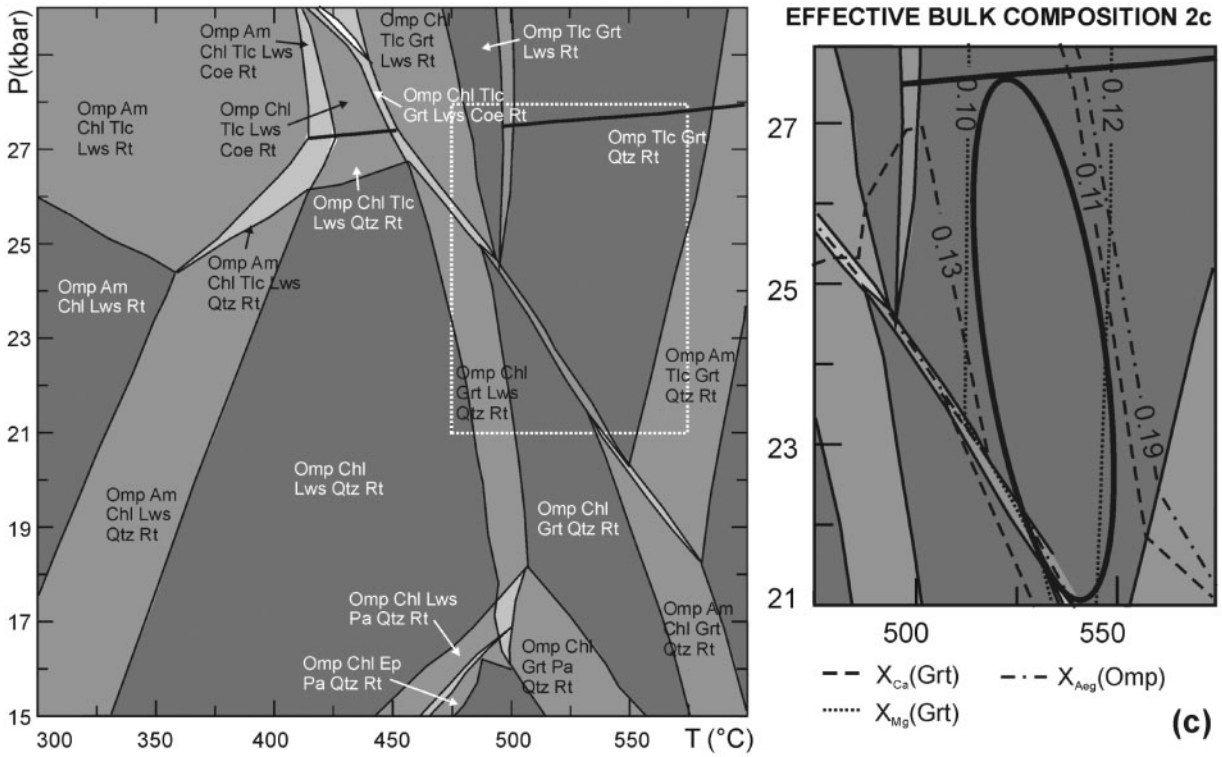

Fig. 5. Continued.

interpreted as earlier than garnet growth; (2) the stability of Gln_1 in the same metamorphic stage. However, additional P–T pseudosection modelling at lower pressure and temperature shows that two clinopyroxenes and glaucophane are stable at $P < 14$ kbar and $T < 300°C$, suggesting that Omp_1, Jd_{ss} and Gln_1 are relics of a prograde assemblage that developed during an earlier stage of subduction.

The studied sample provides little information about its retrograde evolution. Glaucophane in the matrix (Gln_2), which has been interpreted as an early retrograde phase on the basis of microstructural evidence, is predicted to be stable at T slightly higher than the modelled peak conditions (Am in Fig. 5c) and the Gln-in curve has a positive slope. Considering that the modelled peak temperature must be considered as a minimum, the growth of glaucophane appears to be compatible with the earliest stages of retrogression at $P < 23$ kbar and $T < 560°C$. Finally, most of the coarse-grained lawsonite included in garnet has been replaced by epidote + paragonite aggregates (Fig. 2e, g and h). The presence of paragonite in the breakdown assemblage of lawsonite suggests that the reaction is not isochemical. Lü *et al.* (2009) suggested that the required Na could be derived from the jadeite component of the frequent omphacite inclusions in garnet, according to the reaction $Lws + Jd = Czo + Pg + Qtz + H_2O$. There is no evidence of such reaction in the OF2727 sample; however, it is worth noting that epidote + paragonite aggregates replace the coarser-grained lawsonite inclusions, which were most probably polymineralic, whereas the finer-grained monomineralic inclusions are still preserved.

The dehydration reactions

The modelled H_2O amounts at each stage are summarized in Table 5 and Fig. 7a. These data show that the dehydration of the system mainly occurred at the transition between stage I and stage II (Fig. 7a); that is, at the highest T-side of the quini-variant $Lws + Qtz + Chl + Omp + Grt + Rt$ field (Fig. 5b, composition 1e), where the H_2O content decreases from about 3·5 wt % to less than 1·7 wt % (Table 5 and Fig. 7a). The devolatilization reactions responsible for this significant dehydration have been calculated for composition 1e in the simplified system NCFMASHTO at $460 < T < 500°C$, $20 < P < 22$ kbar (i.e. the P–T conditions estimated for the growth of Grt_{1e}). More details on the calculations of dehydration and redox reactions are given in Appendix C.

Because of the approximation by discrete steps of the continuous compositional variation of the involved solution phases (garnet, omphacite and chlorite), the dehydration reactions appear as pseudo-univariant equilibrium curves (Connolly & Kerrick, 1987). Two types of

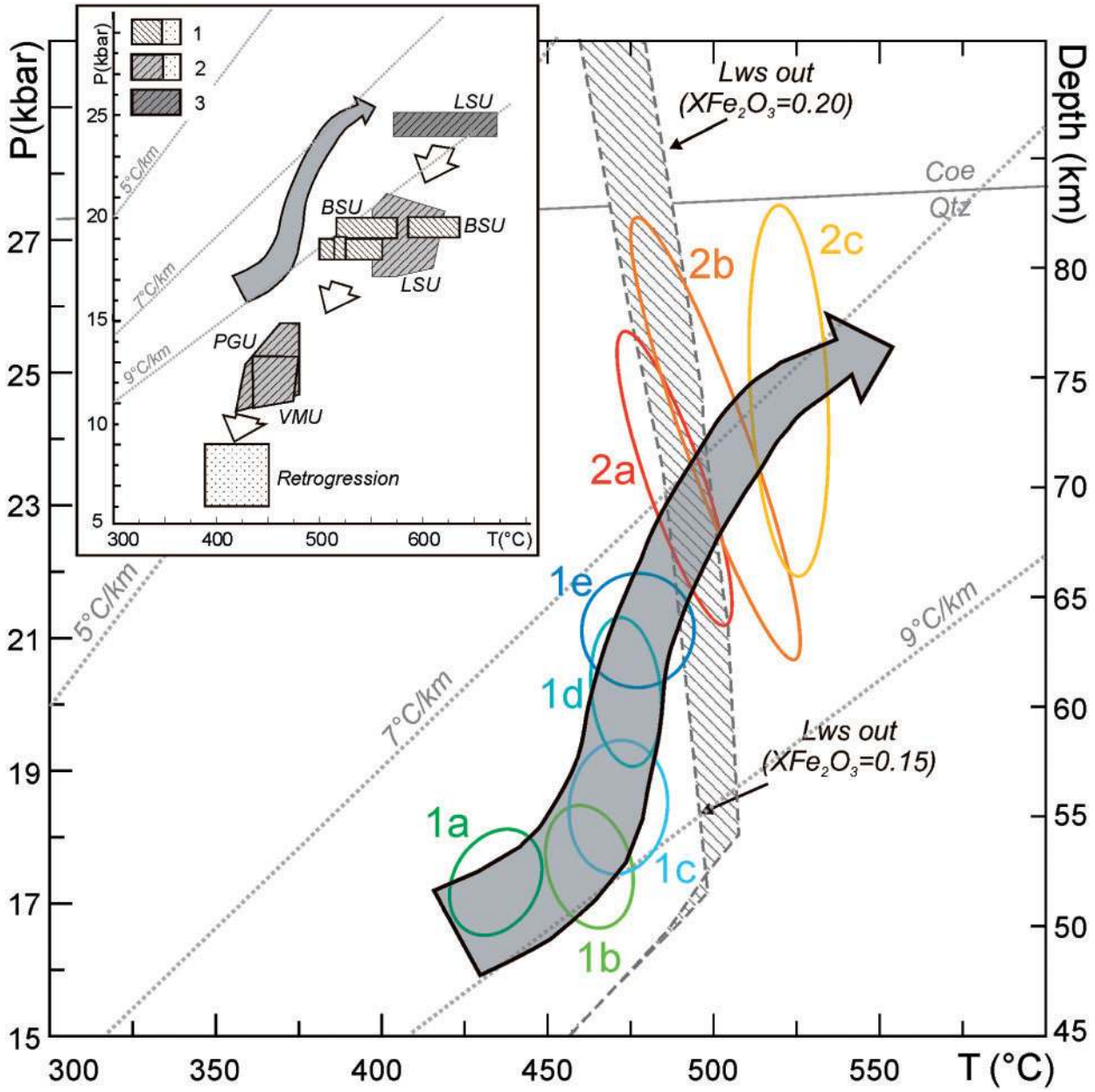

Fig. 6. Prograde P–T path inferred for the studied FeTi-oxide metagabbro. The ellipses refer to P–T conditions constrained by pseudosection analysis for stages I (1a–1e) to II (2a–2c) (see both text and Fig. 5, and Fig. SM7a–d of the Supplementary Material, for further discussion) and document a portion of the prograde P–T path during subduction. The dashed field marks lawsonite breakdown as inferred from pseudosections calculated at $X(Fe_2O_3) = 0{\cdot}20$ and $0{\cdot}15$, for stage I and II, respectively. The dotted curves are thermal gradients. The inset shows the P–T conditions estimated by previous workers for peak (dashed fields: 1, Blake *et al.*, 1995; 2, Schwartz *et al.*, 2000; 3, Messiga *et al.*, 1999) and retrogressive (dotted field) stages in various units of the Monviso meta-ophiolite (abbreviations for units as in Fig. 1); the prograde P–T path inferred from this study is reported for comparison.

pseudo-univariant equilibria occur in the Lws + Qtz + Chl + Omp + Grt + Rt field (Fig. 8):

(A) $Lws + Qtz + Omp_1 + Chl = Omp_2 + Grt + H_2O$;

(B) $Lws + Qtz + Chl_1 + Omp_1 = Chl_2 + Omp_2 + Grt + H_2O$.

Type (A) equilibria are responsible for the breakdown of both lawsonite and chlorite, whereas type (B) equilibria involve the breakdown of lawsonite and a chemical re-equilibration of both omphacite and chlorite. In both equilibria types garnet occurs only as a product, and quartz (present in very low amounts) is completely consumed. The H_2O content of the system rapidly decreases from >3·5 wt % to <1·4 wt % (Fig. 8). For both equilibria types (A) and (B), the breakdown of lawsonite and chlorite

Table 5: Results of the pseudosection modelling

Stage:	Stage I					Stage II		
	1a	1b	1c	1d	1e	2a	2b	2c
Grt: X_{Ca}*	21–24	22–27	21–25	22–18	17–20	13–15	12–14	11–13
Grt: X_{Mg}	1–2	2–3	2–4	3–4	3–5	5–6	6–9	10–12
$X(Fe_2O_3) = 0{\cdot}20$								
T (°C)	425–450	450–475	455–480	460–490	460–490	460–490	470–490	500–520
P (kbar)	16·5–18·5	17–18·5	17·5–19·5	19–21	20–22	23·5–25·5	24·5–27	27–30
Omp: X_{Aeg}	*34–35*	*34–35*	*33–34*	*32–33*	*31–32*	30–31	26–27	26–27
Omp:X_{Jd}	*25–26*	*25–26*	*28–29*	*28–29*	*29–30*	31–32	35–36	36–37
Assemblage†	*Omp(60)*	*Omp(60)*	*Omp(60)*	*Omp(60)*	*Omp(61)*	Omp(62)	Omp(64)	Omp(66)
	Chl(28)	*Chl(27)*	*Chl(27)*	*Chl(26)*	*Chl(25)*	Chl(20)	Grt(14)	Grt(19)
	Lws(7)	*Lws(7)*	*Lws(7)*	*Lws(7)*	*Lws(6)*	Grt(6)	Tlc(7)	Tlc(7)
	Grt(1)	*Rt(4)*	*Rt(4)*	*Rt(4)*	*Rt(4)*	Lws(5)	Chl(6)	Rt(5)
	Rt(4)	*Grt(1)*	*Grt(1)*	*Qtz(2)*	*Grt(2)*	Rt(5)	Rt(5)	Lws(3)
	Qtz(<1)	*Qtz(1)*	*Qtz(1)*	*Grt(1)*	*Qtz(2)*	Qtz(2)	Lws(4)	±Coe(<1)
H_2O wt %	*3·7–3·8*	*3·6–3·7*	*3·4–3·7*	*3·1–3·6*	*2·1–3·5*	2·0–3·3	1·0–2·0	0·5–0·7
$X(Fe_2O_3) = 0{\cdot}15$								
T (°C)	420–440	440–475	450–480	460–490	460–490	470–500	480–520	515–540
P (kbar)	16·5–18	17–18	17·5–19·5	18·5–21	20·5–22	21–25·5	22·5–27	22–27
Omp: X_{Aeg}	24–25	24–25	23–24	23–24	23	*22–23*	*19–20*	*18–19*
Omp: X_{Jd}	32–33	32–33	34–35	34–35	35–36	*37–38*	*40–41*	*41–42*
Assemblage†	Omp(63)	Omp(63)	Omp(63)	Omp(63)	Omp(64)	*Omp(66)*	*Omp(68)*	*Omp(68)*
	Chl(27)	Chl(27)	Chl(26)	Chl(26)	Chl(25)	*Chl(17)*	*Grt(18)*	*Grt(20)*
	Lws(4)	Lws(4)	Rt(4)	Rt(4)	Rt(4)	*Grt(10)*	*Tlc(7)*	*Tlc(7)*
	Rt(4)	Rt(4)	Lws(3)	Lws(3)	Lws(3)	*Rt(5)*	*Rt(5)*	*Rt(5)*
	Grt(1)	Grt(1)	Grt(2)	Grt(2)	Grt(2)	*Qtz(2)*	*Chl(2)*	*Qtz(<1)*
	Qtz(1)	Qtz(1)	Qtz(2)	Qtz(2)	Qtz(2)			
H_2O wt %	3·6–3·7	3·5–3·6	3·4–3·6	3·3–3·5	2·2–3·2	*1·7–2·1*	*0·6–1·2*	*0·3–0·9*

Values in italics represent the best fit between observed and modelled assemblages and phase compositions.
*X_{Ca} and X_{Mg} in garnet, and X_{Aeg} and X_{Jd} in omphacite are ×100.
†The vol. % of each phase is reported in parentheses.

is associated with the growth of garnet and with a significant chemical re-equilibration of omphacite. Compositions of both reactant and product phases vary across the Lws + Qtz + Chl + Omp + Grt + Rt field: with increasing temperature, Chl_2 is more Mg-rich than Chl_1 and, in agreement with the measured compositions, Omp_2 is enriched in the diopsidic component and depleted in the aegirine component with respect to Omp_1, whereas garnet is progressively enriched in the pyrope component (Fig. 8). Intersections between type (A) and (B) pseudo-univariant curves are pseudo-invariant points that mark a change in the composition of chlorite and omphacite along type (A) and (B) equilibria, respectively.

Redox reactions during subduction

To evaluate the redox reactions occurring during the dehydration of the system, an isobaric T–log $f(O_2)$ projection has been calculated at $P = 21$ kbar (i.e. at a pressure averaging the growth of Grt_{1e}) in the simplified system NCFMASHTO (Fig. 9) (see Appendix C for further details).

Because P has been fixed, the pseudo-univariant dehydration equilibria [(A1)–(A9), (B1)–(B4)] of Fig. 8 correspond to pseudo-invariant points in Fig. 9, and they uniquivocally define the log $f(O_2)$ of the assemblage at the given P and T. Changing pressure has a very little influence on the position of the pseudo-invariant points [±0·1 log $f(O_2)$ units for $\Delta P = \pm 1$ kbar]. Figure 9 shows

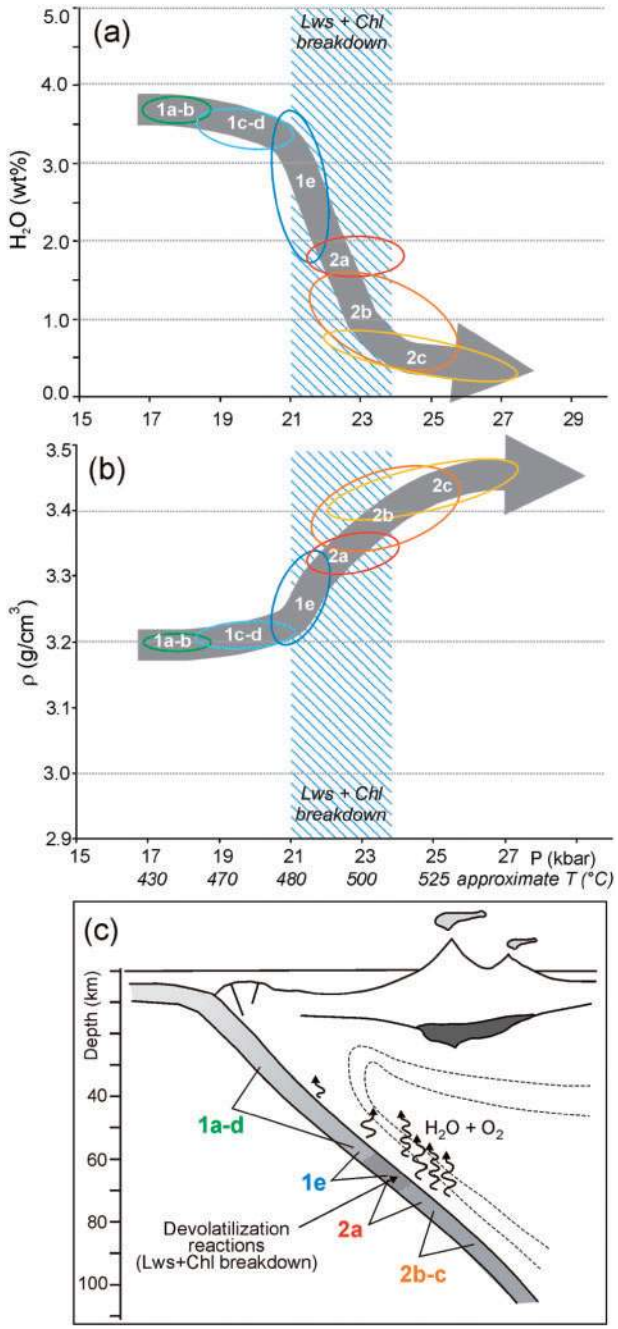

Fig. 7. (a, b) Variations of chemical and physical properties of the FeTi-oxide metagabbro OF2727 during subduction. The diagonal shaded fields mark lawsonite breakdown as inferred from Fig. 6. H_2O content (a) and density (b) values calculated at metamorphic stages I (1a–1e) and II (2a–2c) are reported as a function of *P*. (c) Sketch of metamorphic stages I (1a–1e) and II (2a–2c) of metagabbro OF2727 in the subduction context. The progressively darker grey colour of the subducting oceanic crust implies higher density balanced by lower H_2O content. The darker dashed field along the subducting slab approximates the lawsonite and chlorite breakdown, corresponding to the depth at which the maximum H_2O and O_2 contents are released from the metagabbro into the mantle wedge.

that the log $f(O_2)$ of the system progressively increases [log $f(O_2) = -22{\cdot}8$ to $-20{\cdot}9$] with increasing temperature from stage I to stage II (i.e. the observed Grt_1–Grt_2 and Omp_2–Omp_3 transition).

The pseudo-invariant points [(A1)–(A9), (B1)–(B4)] in the *T*–log $f(O_2)$ projection of Fig. 9 are connected by pseudo-univariant equilibria (*r1*)–(*r12*) that define the more general equilibrium: $Lws + Qtz + Chl_{ss} + Ompl_{ss} = Grt_{ss} + Omp2_{ss} + H_2O + O_2$. The broken shape of this equilibrium is due to the approximation of the continuous variation in the solid-solution compositions by discrete steps (pseudocompounds). Equilibria (*r1*)–(*r12*) correspond to devolatilization reactions that produce H_2O and O_2 up-temperature, and divide the *T*–log $f(O_2)$ space in two fields: on the more oxidized side of the diagram the $Lws + Qtz + Omp_1 + Chl_1$ assemblage is stable, whereas on the more reduced side the $Grt + Omp_2 + H_2O + O_2$ assemblage is stable. Moving along this equilibrium from 460°C to 500°C, chlorite, omphacite and garnet progressively change their compositions. Crossing the $Lws + Qtz + Chl_{ss} + Ompl_{ss} = Grt_{ss} + Omp2_{ss} + H_2O + O_2$ equilibrium towards higher *T*, H_2O and O_2 are released. In particular: (1) for 1 mole of lawsonite + chlorite consumed up *T*, about 2·0–2·7 moles of H_2O are released on average; (2) for 1 mole of omphacite ($Omp2_{ss}$) produced up *T*, about 1 mole of oxygen is released on average (Fig. 9). As a consequence, the resulting assemblage ($Grt_{ss} + Omp2_{ss}$) at $T = 500$°C is less hydrated and less oxidized than the initial one ($Lws + Qtz + Chl_{ss} + Ompl_{ss}$) at $T = 460$°C, accounting for the sharp compositional variation in both omphacite and garnet from stage I to stage II. This means that the $Lws + Qtz + Chl_{ss} + Ompl_{ss} = Grt_{ss} + Omp2_{ss} + H_2O + O_2$ equilibrium represents the boundary between a more oxidized assemblage (at lower *T*) and a more reduced assemblage (at higher *T*).

Reliability of the results

The approach used to infer the *P*–*T*–fO_2 conditions attained during the subduction of the Monviso FeTi-oxide metagabbro deserves some words of caution about the following points.

(1) Although we have demonstrated that a small amount of ferric iron occurs in garnet, the 'well-constrained' Fe^{3+}-free solution model of Holland & Powell (1998) was preferred for pseudosection calculations with respect to the Fe^{3+}-bearing model of White *et al.* (2007). This latter model, in fact, was developed in the pelitic NCKFMASHTO system and the authors themselves warned that the introduction of the end-member thermodynamics and *a*–*x* relationships for spessartine will probably give unreliable or erroneous results if used in conjunction with their model. As garnet cores in the studied sample are considerably richer in Mn than in Fe^{3+}, we have preferred to neglect the

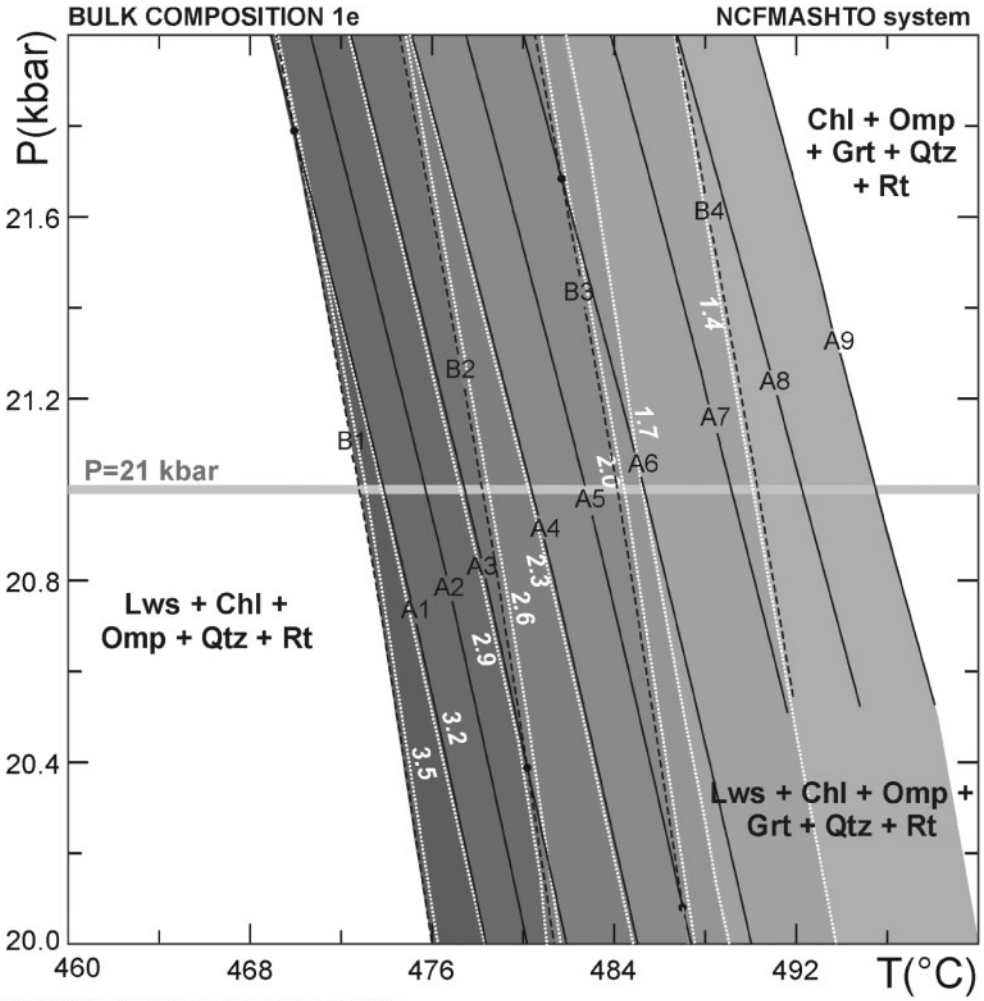

TYPE (A) PSEUDOUNIVARIANT EQUILIBRIA

(A1) Lws + Qtz + Omp_1(Di20Jd30Aeg32) + Chl(Daph64) = *Omp_2(Di21Jd29Aeg31)* + Grt(Alm80Prp4) + H_2O
(A2) Lws + Qtz + *Omp_1(Di22Jd30Alm31)* + Chl(Daph64) = Omp_2*(Di23Jd29Aeg31)* + Grt(Alm80Prp4) + H_2O
(A3) Lws + Qtz + *Omp_1(Di22Jd29Aeg32)* + Chl(Daph64) = *Omp_2(Di24Jd29Aeg31)* + Grt(Alm80Prp4) + H_2O
(A4) Lws + Qtz + Omp_1(Di22Jd30Aeg32) + Chl(Daph60) = *Omp_2(Di24Jd29Aeg31)* + Grt(Alm80Prp4) + H_2O
(A5) Lws + Qtz + *Omp_1(Di24Jd30Alm31)* + Chl(Daph60) = *Omp_2(Di25Jd29Aeg31)* + Grt(Alm80Prp4) + H_2O
(A6) Lws + Qtz + *Omp_1(Di25Jd29Aeg31)* + Chl(Daph56) = *Omp_2(Di25Jd29Aeg32)* + Grt(Alm78Prp4) + H_2O
(A7) Lws + Qtz + Omp_1(Di24Jd30Aeg32) + Chl(Daph56) = *Omp_2(Di26Jd29Aeg31)* + Grt(Alm78Prp6) + H_2O
(A8) Lws + Qtz + *Omp_1(Di26Jd30Aeg31)* + Chl(Daph52) = *Omp_2(Di27Jd29Aeg31)* + Grt(Alm78Prp6) + H_2O
(A9) Lws + Qtz + *Omp_1(Di26Jd29Aeg32)* + Chl(Daph52) = *Omp_2(Di28Jd29Aeg31)* + Grt(Alm78Prp6) + H_2O

TYPE (B) PSEUDOUNIVARIANT EQUILIBRIA

(B1) Lws + Qtz + Chl_1(Daph68) + Omp_1(Di20Jd30Aeg32) = Chl_2(Daph64) + *Omp_2(Di22Jd29Aeg31)* + Grt(Alm80Prp4) + H_2O
(B2) Lws + Qtz + Chl_1(Daph64) + Omp_1(Di21Jd30Aeg32) = Chl_2(Daph60) + *Omp_2(Di24Jd29Aeg31)* + Grt(Alm80Prp4) + H_2O
(B3) Lws + Qtz + Chl_1(Daph60) + *Omp_1(Di25Jd29Aeg31)* = Chl_2(Daph56) + Omp_2(Di24Jd30Aeg32) + Grt(Alm78Prp4) + H_2O
(B4) Lws + Qtz + Chl_1(Daph56) + Omp_1(Di26Jd30Aeg32) = Chl_2(Daph52) + *Omp_2(Di26Jd29Aeg31)* + Grt(Alm78Prp6) + H_2O

Fig. 8. *P–T* pseudosection calculated in the simplified system NCFMASHTO at $a(H_2O) = 1$ and $X(Fe_2O_3) = 0{\cdot}20$, using the effective bulk composition le (see Table 4), in the *P–T* range constrained for stage le ($T = 460$–$500°C$, $P = 20$–22 kbar). The grey field is the quini-variant Lws + Chl + Omp + Grt + Qtz + Rt field of Fig. 5b, with darker and lighter grey corresponding to higher and lower H_2O amounts, respectively. H_2O isomodes are reported as white dotted lines. Differences with respect to Fig. 5b are due to the simplified model system (see Appendix C for discussion). Type (A) and (B) pseudo-univariant dehydration equilibria (see text for discussion) are indicated as continuous and dashed lines, respectively. Black dots are pseudo-invariant points. The listed equilibria are written such that the higher-*T* assemblages are on the right. Because of the approximation by discrete steps of the continuous variation in the composition of solid-solutions, the composition of phases in italics is the average of two or three pseudocompounds. The horizontal light grey line at 21 kbar marks the isobaric section reported in Fig. 9. Solid-solution compositions: Di = diopside, Jd = jadeite, Aeg = aegirine (hedenbergite as difference to 100) for omphacite; Daph = daphnite (clinochlore as difference to 100) for chlorite; Alm = almandine; Prp = pyrope (grossular as difference to 100) for garnet.

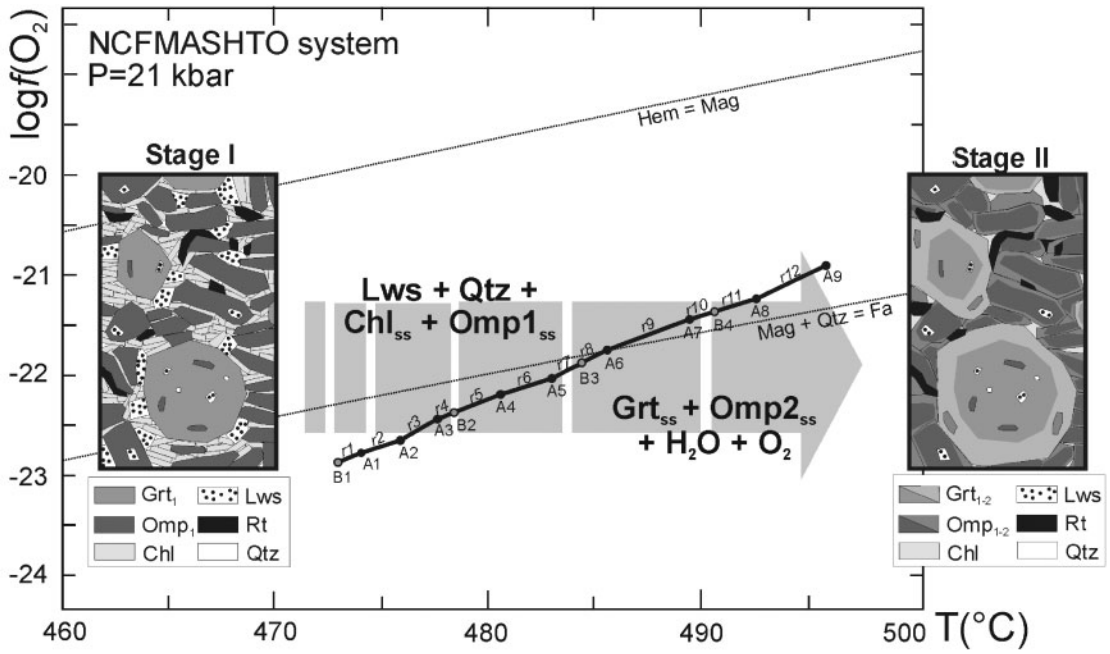

(*r1*) 0.2 Lws + 0.2 Qtz + 0.1 Chl(Daph64) + 14.3 *Omp$_1$(Di21Jd29Aeg32)* = 0.2 Grt(Alm80Prp4) + 14.5 Omp$_2$(Di22Jd30Aeg30) + 0.8 H_2O + 0.1 O_2
(*r2*) 0.2 Lws + 0.1 Qtz + 0.02 Chl(Daph64) + 14.3 *Omp$_1$(Di22Jd29Aeg32)* = 0.1 Grt(Alm80Prp4) + 14.4 Omp$_2$(Di22Jd30Aeg30) + 0.5 H_2O + 0.1 O_2
(*r3*) 0.4 Lws + 0.3 Qtz + 0.2 Chl(Daph64) + 14.5 *Omp$_1$(Di22Jd29Aeg32)* = 0.5 Grt(Alm80Prp4) + 14.6 Omp$_2$(Di24Jd30Aeg30) + 1.6 H_2O + 0.1 O_2
(*r4*) 0.2 Lws + 0.2 Qtz + 0.1 Chl(Daph64) + 14.3 *Omp$_1$(Di23Jd29Aeg32)* = 0.2 Grt(Alm80Prp4) + 14.5 Omp$_2$(Di24Jd30Aeg30) + 0.8 H_2O + 0.1 O_2
(*r5*) 0.5 Lws + 0.2 Qtz + 0.1 Chl(Daph60) + 24.7 *Omp$_1$(Di23Jd29Aeg32)* = 0.2 Grt(Alm80Prp4) + 25.0 Omp$_2$(Di24Jd30Aeg30) + 1.2 H_2O + 0.1 O_2
(*r6*) 0.2 Lws + 0.1 Qtz + 0.02 Chl(Daph60) + 14.3 *Omp$_1$(Di24Jd29Aeg32)* = 0.1 Grt(Alm80Prp4) + 14.4 Omp$_2$(Di24Jd30Aeg30) + 0.4 H_2O + 0.1 O_2
(*r7*) 0.3 Lws + 0.2 Qtz + 0.2 Chl(Daph60) + 13.7 Omp$_1$(Di24Jd28Aeg32) = 0.4 Grt(Alm78Prp4) + 13.8 *Omp$_2$(Di26Jd29Aeg30)* + 1.4 H_2O + 0.1 O_2
(*r8*) 0.3 Lws + 0.2 Qtz + 0.2 Chl(Daph56) + 13.9 *Omp$_1$(Di24Jd29Aeg32)* = 0.4 Grt(Alm78Prp4) + 14.0 Omp$_2$(Di26Jd30Aeg30) + 1.3 H_2O + 0.1 O_2
(*r9*) 0.2 Lws + 0.1 Qtz + 0.1 Chl(Daph56) + 14.3 *Omp$_1$(Di25Jd29Aeg32)* = 0.2 Grt(Alm78Prp6) + 14.5 Omp$_2$(Di26Jd30Aeg30) + 0.7 H_2O + 0.1 O_2
(*r10*) 0.2 Lws + 0.1 Qtz + 0.02 Chl(Daph56) + 14.3 *Omp$_1$(Di26Jd29Aeg32)* = 0.1 Grt(Alm78Prp6) + 14.5 Omp$_2$(Di26Jd30Aeg30) + 0.5 H_2O + 0.1 O_2
(*r11*) 0.2 Lws + 0.1 Qtz + 0.02 Chl(Daph52) + 14.3 *Omp1(Di26Jd29Aeg32)* = 0.1 Grt(Alm78Prp6) + 14.4 Omp$_2$(Di26Jd30Aeg30) + 0.4 H_2O + 0.1 O_2
(*r12*) 0.3 Lws + 0.2 Qtz + 0.2 Chl(Daph52) + 14.4 Omp$_1$(*Di26Jd29Aeg32*) = 0.4 Grt(Alm78Prp6) + 14.6 Omp$_2$(Di28Jd30Aeg30) + 1.3 H_2O + 0.1 O_2

Fig. 9. Isobaric T–log $f(O_2)$ section in the NCFMASHTO system at P–T conditions constrained for stage 1e (i.e. average $P = 21$ kbar and $460 < T < 500$°C). Pseudo-invariant points A1–A9 and B1–B4 correspond to the pseudo-univariant dehydration equilibria of Fig. 8 (see text for details), and are connected by the pseudo-univariant redox equilibria (*r1*)–(*r12*). Equilibria (*r1*)–(*r12*) define the general redox equilibrium $Lws + Qtz + Chl_{ss} + Ompl_{ss} = Grt_{ss} + Omp2_{ss} + H_2O + O_2$ (the broken shape is due to the pseudocompounds approximation), which divides the T–log $f(O_2)$ space into two fields (the more oxidized $Lws + Qtz + Chl_{ss} + Ompl_{ss}$ field, at lower T, and the more reduced $Grt_{ss} + Omp2_{ss} + O_2$ field, at higher T, respectively). The magnetite + quartz = fayalite and hematite = magnetite buffers are shown for comparison. The two insets schematically represent the metamorphic assemblages before (stage I) and after (stage II) the breakdown of lawsonite and chlorite. The grey arrow schematically shows the evolution from the more oxidized assemblage (stage I) to the more reduced assemblage (stage II) related to lawsonite and chlorite breakdown. All the listed equilibria are written such that the higher-T assemblages are on the right. Because of the approximation of the continuous variation in the solid-solution compositions by discrete steps, the composition of phases in italics is the average of two or three pseudocompounds. Abbreviations for solid-solution compositions are the same as in Fig. 8.

influence of Fe^{3+} for the stabilization of garnet. This choice mainly affects the P–T conditions estimated for the Grt_1 growth stages, which contain the maximum Fe^{3+} contents (especially $Grt_{1a\text{-}c}$, for which $Fe^{3+}/\Sigma Fe > 0{\cdot}05$), and probably results in some underestimation of the P–T conditions (about 1 kbar and 10°C, respectively) inferred for the growth of garnet cores.

(2) The $Fe^{3+}/\Sigma Fe$ ratio in omphacite has not been directly measured but only calculated by stoichiometry from electron microprobe (EMP) analyses. Previous studies (e.g. Sobolev *et al.*, 1999; Schmid *et al.*, 2003; Proyer *et al.*, 2004) have demonstrated that in many cases there is no direct correlation between EMP-calculated values and values measured using other techniques such as Mössbauer or micro-XANES (X-ray absorption near edge structure) spectroscopy. This could obviously affect the validity of our results, which are also based on the best fit between modelled and calculated omphacite compositions. In omphacite, the precision in the determination of SiO_2 and Na_2O largely

controls the $Fe^{3+}/\Sigma Fe$ values based on stoichiometry (e.g. Sobolev *et al.*, 1999). Omphacite crystals in the studied sample have been analysed using both wavelength-dispersive (WDS) and energy-dispersive (EDS) techniques, with various analytical conditions and calibration standards: the X_{Aeg} and X_{Jd} ratios calculated by stoichiometry from the two set of analyses are comparable (WDS—Omp_2: $X_{Jd} = 0{\cdot}24$–$0{\cdot}34$, $X_{Aeg} = 0{\cdot}30$–$0{\cdot}35$; Omp_3: $X_{Jd} = 0{\cdot}36$–$0{\cdot}38$, $X_{Aeg} = 0{\cdot}17$–$0{\cdot}18$; EDS—Omp_2: $X_{Jd} = 0{\cdot}28$–$0{\cdot}32$, $X_{Aeg} = 0{\cdot}31$–$0{\cdot}33$; Omp_3: $X_{Jd} = 0{\cdot}38$–$0{\cdot}39$, $X_{Aeg} = 0{\cdot}18$–$0{\cdot}19$). In addition, special care has been taken in determining the Na content using the WDS technique, by decreasing the acquisition time to avoid Na loss. We are therefore confident that the calculated $Fe^{3+}/\Sigma Fe$ ratios are a reliable approximation of the actual redox state of omphacite.

(3) Pseudosection modelling suggests that chlorite was stable during the prograde evolution. As is the case for other phyllosilicates, the substitution of Al^{3+} for Fe^{3+} may also occur in chlorite and the presence of Fe^{3+} will affect the activity of chlorite end-members. However, it has been neglected in the modelling because of the lack of thermodynamic data for the Fe^{3+}-chlorite end-member. Vidal *et al.* (2006) demonstrated that there is a strong correlation between the Fe^{3+} content of chlorite and temperature, and that only at $T < 250°C$ is the $Fe^{3+}/\Sigma Fe$ ratio of chlorite higher than 0·10. We are therefore confident that, at the temperatures considered in the modelling ($T > 400°C$), the influence of Fe^{3+} in chlorite can be neglected.

DISCUSSION

The *P–T* evolution of the Basal Serpentinite Unit

The exceptionally well-preserved prograde assemblage of the studied eclogite-facies FeTi-oxide metagabbro has allowed us to reconstruct in detail a segment of the Basal Serpentinite Unit prograde evolution, from about 420°C, 16 kbar to peak conditions of ≥550°C, 25–26 kbar (Fig. 6). The first stages of evolution (i.e. growth of Grt_{1a-1c}) should be considered with care, because a number of problems could induce uncertainties in the reliability of the constrained *P–T* conditions (see the above discussion). The estimated peak conditions are very similar to those obtained by Messiga *et al.* (1999) for a chloritoid + talc-bearing metagabbro from the Lago Superiore Unit, structurally upward in the Monviso meta-ophiolites, whereas *P* estimates are considerably higher than those proposed by Blake *et al.* (1995) for the same Basal Serpentinite Unit. However, pressures obtained by Blake *et al.* (1995) were only minimum pressures, because they were based on the Jd-in-omphacite barometer.

Previous researchers did not report *P–T* constraints for the prograde stages of metamorphism in the Monviso meta-ophiolites: thus, in this study we propose the first reconstruction of the prograde evolution for a Monviso unit. Our data show that subduction occurred along very low thermal gradients, typical of cold subduction zones and compatible with lawsonite formation (e.g. Liou *et al.*, 2004). In more detail, it is evident that the thermal gradient changed through time during subduction, decreasing from about 9°C km^{-1} to less than 7°C km^{-1} (assuming an average density of 3·0 g cm^{-3}) (Fig. 6). A similar decrease of the thermal gradient in the oceanic Piedmonte Zone subducting slab has been described in the Zermatt–Saas Zone of the Western Alps for the ultrahigh-pressure Lago di Cignana Unit and its adjoining units (Groppo *et al.*, 2009*a*), and interpreted as the evidence of a progressive increase in the subduction rate. This interpretation is consistent with observations and models that require a significant length of slab to be present at mantle depths to act as an engine for subduction (Royden & Husson, 2006).

The lawsonite breakdown during subduction and the devolatilization reactions

The data presented in this study show that eclogitization of the studied metagabbro was accompanied by a significant prograde loss of fluids, mainly related to the breakdown of lawsonite and chlorite. This conclusion is in line with the results of Philippot & Selverstone (1991) and Nadeau *et al.* (1993) on similar rocks from the same area (Lago Superiore Unit, directly overlying the Basal Serpentinite Unit). However, the new *P–T* constraints provided by the pseudosection modelling allow us to conclude that most of these fluids were released at a depth of about 65–70 km, a considerably greater depth than that estimated by those workers (*c.* 40 km). Our results are also consistent with those of Lü *et al.* (2009), who recognized two critical dehydration processes (related to the breakdown of chlorite and glaucophane + lawsonite, respectively) during subduction of UHP coesite-bearing eclogites from Tianshan.

Reactions responsible for lawsonite breakdown have been experimentally investigated for both basaltic and andesitic compositions (Poli & Schmidt, 1995; Okamoto & Maruyama, 1999). Experimental results suggest that, at pressures higher than the zoisite/clinozoisite stability field, the destabilization of lawsonite results in assemblages composed of anhydrous minerals; that is, garnet + clinopyroxene + quartz/coesite ± kyanite (Poli & Schmidt, 1995; Okamoto & Maruyama, 1999). Lawsonite disappearance in the basaltic system under H_2O-saturated conditions is ascribed to a continuous reaction of the type $Lws + Cpx + Grt_1 = Grt_2 + Qtz/Coe + H_2O$ [reaction (2) of Poli & Schmidt (1995)], where garnet progressively

shifts towards grossular-rich compositions along a prograde P–T path (Okamoto & Maruyama, 1999; Poli *et al.*, 2009).

The studied FeTi-oxide metagabbro OF2727 has a bulk composition that differs from a common basaltic composition, being significantly enriched in both Fe and Ti (FeO_{tot} ~21 wt %, TiO_2 ~5·5 wt %). Therefore, different reactions controlling lawsonite breakdown are expected. Microstructural and mineral chemical observations suggest that both garnet and omphacite compositions significantly changed during lawsonite breakdown (i.e. the Grt_1 to Grt_2 and Omp_2 to Omp_3 transitions coincide with the disappearance of lawsonite; see Table 3). However, contrary to the experimental data of Poli & Schmidt (1995), Okamoto & Maruyama (1999) and Poli *et al.* (2009), the grossular content of garnet sharply decreases simultaneously with lawsonite disappearance. The dehydration reactions modelled for the metagabbro composition [i.e. equilibria (A1)–(A9) and (B1)–(B4) of Fig. 8] suggest that (1) quartz is always a reactant [whereas it is a product in the reactions proposed by Poli & Schmidt (1995) and Okamoto & Maruyama (1999)] and (2) chemical re-equilibration of omphacite (and not of garnet) is involved in the dehydration process. In particular, omphacite becomes enriched in the diopsidic component (Fig. 8) up temperature, thus suggesting that the Ca released from lawsonite is exchanged with clinopyroxene instead of garnet. Therefore, comparing our results with the experimental data, we suggest that the bulk composition of the system could have a strong influence on the dehydration reactions occurring during subduction.

Changing redox state of the FeTi-oxide metagabbro during subduction

Our modelling suggests that the dehydration equilibria involved in lawsonite and chlorite breakdown also release O_2, thus controlling the redox state of the system during subduction (Fig. 9). This result has interesting implications for understanding the complex interactions between crust and mantle in subduction zones. Slab-derived fluid phases have been suggested as the agents for the oxidized nature of the mantle wedge compared with the oceanic mantle, as evidenced by (1) strongly oxidized xenoliths coming from subduction-related areas (Wood *et al.*, 1990; Carmichael, 1991; Ballhaus, 1993; Parkinson & Arculus, 1999; Peslier *et al.*, 2002) and (2) oxygen fugacity data from orogenic peridotites (Malaspina *et al.*, 2009). Although it is accepted that the mantle wedge above subduction zones is oxidized, the exact processes of relative oxidation are still controversial (e.g. Parkinson & Arculus, 1999; Malaspina *et al.*, 2009; Rowe *et al.*, 2009). However, it is widely recognized that oxidized components are transferred to the overlying mantle wedge by fluids and/or melts coming from the subducting slab (e.g. Parkinson & Arculus, 1999; Peslier *et al.*, 2002; Malaspina *et al.*, 2009; Rowe *et al.*, 2009). H_2O-rich fluids have been alternatively interpreted as very effective oxidizing agents (Brandon & Draper, 1996, 1998) or as extremely poor oxidizing agents (Ballhaus, 1993; Frost & Ballhaus, 1998). According to the first hypothesis (Brandon & Draper, 1996), water may be an oxidizing agent because, after dissociation, oxygen forms ferric iron and hydrogen escapes the system. Conversely, Frost & Ballhaus (1998) argued that the very low H_2O dissociation constant hampers its oxidizing capability. According to our data, the oxidation of the mantle wedge may be triggered by dehydration–redox reactions that occur, at least locally, in the subducting slab. This hypothesis must be considered as preliminary, as FeTi-oxide metagabbros are minor components of the subducting slab. However, our results represent a contribution to clarify if and how the metamorphic transformations occurring in the subducting slab play a role in the oxidation of the overlying mantle wedge.

Published Fe^{3+} data on omphacite in other FeTi-oxide metagabbros from the Western Alps (Pognante, 1985; Pognante & Kienast, 1987) also show prograde omphacite enriched in Fe^{3+} with respect to peak omphacite, thus suggesting, at least for this kind of protolith, the existence of a correlation between decreasing Fe^{3+} in omphacite and increasing metamorphic grade. Further and complementary work on other representative lithologies (metabasalts and MgAl-metagabbros) from similar palaeosubduction zones is needed to generalize this result to the whole subducting slab.

ACKNOWLEDGEMENTS

Careful and constructive reviews by K. Bucher, G. Godard and T. Tsujimori were greatly appreciated, as well as the in-depth comments, suggestions and editorial handling by J. Hermann. We also gratefully acknowledge S. Poli and two anonymous reviewers for their constructive reviews of a preliminary version of the manuscript, J. Connolly and B. Cesare for useful discussions and suggestions, and N. Malaspina for providing Fig. SM3c. N. Malaspina and A. Risplendente helped in acquiring the $Fe^{3+}/\Sigma Fe$ and microprobe data at the Department of Earth Sciences, University of Milan (Italy).

FUNDING

The instrument used for the μ-XRF maps was acquired by the Interdepartmental Center 'G. Scansetti' for Studies on Asbestos and Other Toxic Particulates with a grant from Compagnia di San Paolo, Torino, Italy. This work is part of a PRIN2008 research project on subduction zones of Periadriatic chains funded by the Italian Ministry of Universities and Research.

SUPPLEMENTARY DATA

Supplementary data for this paper are available at *Journal of Petrology* online.

REFERENCES

Ballhaus, C. (1993). Oxidation states of the lithospheric and asthenospheric upper mantle. *Contributions to Mineralogy and Petrology* **114**, 331–348.

Blake, C., Moore, D. G. & Jayko, A. S. (1995). The role of the serpentinite melange in the unroofing of the UHP rocks: an example from the western Alps in Italy. In: Coleman, R. G. & Wang, X. (eds) *Ultrahigh Pressure Metamorphism*. Cambridge: Cambridge University Press, pp. 182–205.

Bocchio, R., Benciolini, L., Martin, S. & Tartarotti, P. (2000). Geochemistry of eclogitised Fe–Ti gabbros from various lithological settings (Aosta Valley ophiolites, Italian western Alps). Protolith composition and eclogitic paragenesis. *Periodico di Mineralogia* **69**, 217–237.

Brandon, A. D. & Draper, D. S. (1996). Constraints on the origin of the oxidation state of mantle overlying subduction zones: an example from Simcoe, Washington, USA. *Geochimica et Cosmochimica Acta* **60**, 1739–1749.

Brandon, A. D. & Draper, D. S. (1998). Reply to the comment by B. R. Frost and C. Ballhaus on 'Constraints on the origin of the oxidation state of mantle overlying subduction zones: an example from Simcoe, Washington, USA'. *Geochimica et Cosmochimica Acta* **62**, 333–335.

Bucher, M. & Frey, K. (2002). *Petrogenesis of Metamorphic Rocks*, 7th edn. Berlin: Springer, 341 p.

Carmichael, I. S. E. (1991). The oxidation state of basic magmas: a reflection of their source regions? *Contributions to Mineralogy and Petrology* **106**, 129–142.

Carson, C. J., Powell, R. & Clarke, G. L. (1999). Calculated mineral equilibria for eclogites in CaO–Na_2O–FeO–MgO–Al_2O_3–SiO_2–H_2O: application to the Pouebo Terrane, Pam Peninsula, New Caledonia. *Journal of Metamorphic Geology* **17**, 9–24.

Castelli, D. & Lombardo, B. (2007). The plagiogranite–FeTi-oxide gabbro association of Vernè (Monviso metamorphic ophiolite, Western Alps). *Ofioliti* **32**, 1–14.

Castelli, D., Rostagno, C. & Lombardo, B. (2002). Jd–Qtz-bearing metaplagiogranite from the Monviso meta-ophiolite (Western Alps). *Ofioliti* **27**, 81–90.

Clarke, G. L., Aitchison, J. C. & Cluzel, D. (1997). Eclogites and blueschists of the Pam Peninsula, NE New Caledonia: a reappraisal. *Journal of Petrology* **38**, 843–876.

Clarke, G. L., Powell, R. & Fitzherbert, J. (2006). The lawsonite paradox: a comparison of field evidence and mineral equilibria modelling. *Journal of Metamorphic Geology* **24**, 715–725.

Clift, P. D., Rose, E. F., Shimizu, N., Layne, G. D., Draut, A. E. & Regelous, M. (2001). Tracing the evolving flux from the subducting plate in the Tonga–Kermadec arc system using boron in volcanic glass. *Geochimica et Cosmochimica Acta* **65**, 3347–3364.

Connolly, J. A. D. (1990). Multivariable phase diagrams: an algorithm based on generalized thermodynamics. *American Journal of Science* **290**, 666–718.

Connolly, J. A. D. (2009). The geodynamic equation of state: what and how. *Geochemistry, Geophysics, Geosystems* **10**, Q10014.

Connolly, J. A. D. & Kerrick, D. M. (1987). An algorithm and computer program for calculating computer phase diagrams. *CALPHAD* **11**, 1–55.

Cossio, R., Borghi, A. & Ruffini, R. (2002). Quantitative modal determination of geological samples based on X-ray multielemental map acquisition. *Microscopy and Microanalysis* **8**, 139–149.

Dasgupta, R. & Hirschmann, M. M. (2006). Melting in the Earth's deep upper mantle caused by carbon dioxide. *Nature* **440**, 659–662.

Dasgupta, R., Hirschmann, M. M. & Withers, A. C. (2004). Deep global cycling of carbon constrained by the solidus of anhydrous, carbonated eclogite under upper mantle conditions. *Earth and Planetary Science Letters* **227**, 73–85.

Davis, P. B. & Whitney, D. L. (2006). Petrogenesis of lawsonite and epidote eclogite and blueschist, Sivrihisar Massif, Turkey. *Journal of Metamorphic Geology* **24**, 823–849.

Davis, P. B. & Whitney, D. L. (2008). Petrogenesis and structural petrology of high pressure metabasalt pods, Sivrihisar, Turkey. *Contributions to Mineralogy and Petrology* **156**, 217–241.

Diener, J. F. A., Powell, R., White, R. W. & Holland, T. J. B. (2007). A new thermodynamic model for clino- and orthoamphiboles in the system Na_2O–CaO–FeO–MgO–Al_2O_3–SiO_2–H_2O–O. *Journal of Metamorphic Geology* **25**, 631–656.

Evans, T. P. (2004). A method for calculating effective bulk composition modification due to crystal fractionation in garnet-bearing schist: implication for isopleth thermobarometry. *Journal of Metamorphic Geology* **22**, 547–557.

Forneris, J. F. & Holloway, J. R. (2003). Phase equilibria in subducting basaltic crust: implications for H_2O release from the slab. *Earth and Planetary Science Letters* **214**, 187–201.

Frost, B. R. & Ballhaus, C. (1998). Comment on 'Constraints on the origin of the oxidation state of mantle overlying subduction zones: an example from Simcoe, Washington, USA'. *Geochimica et Cosmochimica Acta* **62**, 329–331.

Gaidies, F., Abart, R., De Capitani, C., Schuster, R., Connolly, J. A. D. & Reusser, E. (2006). Characterization of polymetamorphism in the Austroalpine basement east of the Tauern Window using garnet isopleth thermobarometry. *Journal of Metamorphic Geology* **24**, 451–475.

Ghent, E., Tinkham, D. & Marr, R. (2009). Lawsonite eclogites from the Pinchi Lake area, British Columbia: new P–T estimates and interpretation. *Lithos* **109**, 248–253.

Green, E. C. R., Holland, T. J. B. & Powell, R. (2007). An order–disorder model for omphacitic pyroxenes in the system jadeite–diopside–hedenbergite–acmite, with applications to eclogitic rocks. *American Mineralogist* **92**, 1181–1189.

Groppo, C., Lombardo, B., Castelli, D. & Compagnoni, R. (2007). Exhumation history of the UHPM Brossasco–Isasca Unit, Dora–Maira Massif, as inferred from a phengite–amphibole eclogite. *International Geology Review* **49**, 142–168.

Groppo, C., Beltrando, M. & Compagnoni, R. (2009*a*). P–T path of the UHP Lago di Cignana and adjoining HP meta-ophiolitic units: insights into the evolution of subducting Tethyan slab. *Journal of Metamorphic Geology* **27**, 207–231.

Groppo, C., Forster, M., Lister, G. & Compagnoni, R. (2009*b*). Glaucophane schist and associated rocks from Sifnos (Cyclades, Greece): new constraints on the P–T evolution from oxidized systems. *Lithos* **109**, 254–273.

Groppo, C. & Rolfo, F. (2008). P–T evolution of the Aghil Range between Kunlun and Karakorum (SW Sinkiang, China). *Lithos* **105**, 365–378.

Hacker, B. R., Abers, G. A. & Peacock, S. M. (2003). Subduction factory: 1. Theoretical mineralogy, densities, seismic wave speeds, and H2O contents. *Journal of Geophysical Research* **108**, ESE 10/1–10/26.

Hawkesworth, C. J., Gallagher, K., Hergt, J. M. & McDermott, F. (1993). Mantle and slab contributions in arc magmas. *Annual Review of Earth and Planetary Sciences* **21**, 175–204.

Höfer, H. E. & Brey, G. P. (2007). The iron oxidation state of garnet by electron microprobe: its determination with the flank method combined with major-element analysis. *American Mineralogist* **92**, 873–885.

Höfer, H. E., Bry, G. P., Schulz-Dobrick, B. & Oberhänsli, R. (1994). The determination of the oxidation state of iron by the electron microprobe. *European Journal of Mineralogy* **6**, 407–418.

Holland, T., Baker, J. & Powell, R. (1998). Mixing properties and activity–composition relationships of chlorites in the system MgO–FeO–Al_2O_3–SiO_2–H_2O. *European Journal of Mineralogy* **10**, 395–406.

Holland, T. J. B. & Powell, R. (1998). An internally consistent thermodynamic data set for phases of petrologic interest. *Journal of Metamorphic Geology* **16**, 309–343.

Kerrick, D. M. & Connolly, J. A. D. (1998). Subduction of ophicarbonates and recycling of CO_2 and H_2O. *Geology* **26**, 375–378.

Kerrick, D. M. & Connolly, J. A. D. (2001*a*). Metamorphic devolatilization of subducted marine sediments and the transport of volatiles into the Earth's mantle. *Nature* **411**, 293–295.

Kerrick, D. M. & Connolly, J. A. D. (2001*b*). Metamorphic devolatilization of subducted oceanic metabasalts: implications for seismicity, arc magmatism and volatile recycling. *Earth and Planetary Science Letters* **189**, 19–29.

Korzhinskii, D. S. (1959). *Physicochemical basis of the analysis of the paragenesis of minerals*. New York: Consultants Bureau, 19 p.

Lagabrielle, Y. & Lemoine, M. (1997). Alpine, Corsican and Apennine ophiolites: the slow-spreading ridge model. *Comptes Rendus de l'Académie des Sciences, Série IIA* **325**, 909–920.

Leake, B. E., Woolley, A. R., Arps, C. E. S., Birch, W. D. *et al.* (1997). Nomenclature of amphiboles: Report of the Subcommittee on Amphiboles of the International Mineralogical Association, Commission on New Minerals and Mineral Names. *American Mineralogist* **82**, 1019–1037.

Liou, J. G., Tsujimori, T., Zhang, R. Y., Katayama, I. & Maruyama, S. (2004). Global UHP metamorphism and continental subduction/collision: The Himalayan model. *International Geology Review* **46**, 1–27.

Liu, J., Bohlen, S. R. & Ernst, W. G. (1996). Stability of hydrous phases in subducting oceanic crust. *Earth and Planetary Science Letters* **143**, 161–171.

Lombardo, B., Nervo, R., Compagnoni, R., Messiga, B., Kienast, J. R., Mével, C., Fiora, L., Piccardo, G. B. & Lanza, R. (1978). Osservazioni preliminari sulle ofioliti metamorfiche del Monviso (Alpi Occidentali). *Rendiconti della Società Italiana di Mineralogia e Petrologia* **34**, 253–305.

Lombardo, B., Rubatto, D. & Castelli, D. (2002). Ion microprobe U–Pb dating of zircon from a Monviso metaplagiogranite: Implications for the evolution of the Piedmont–Liguria Tethys in the Western Alps. *Ofioliti* **27**, 109–117.

Lü, Z., Zhang, L., Du, J. & Bucher, K. (2009). Petrology of coesite-bearing eclogite from Habutengsu Valley, western Tianshan, NW China and its tectonometamorphic implication. *Journal of Metamorphic Geology* **27**, 773–787.

Malaspina, N., Poli, S. & Fumagalli, P. (2009). The oxidation state of metasomatized mantle wedge: insights from C–O–H-bearing garnet peridotite. *Journal of Petrology* **50**, 1533–1552.

Marmo, B. A., Clarke, G. L. & Powell, R. (2002). Fractionation of bulk rock composition due to porphyroblast growth; effects on eclogite facies mineral equilibria, Pam Peninsula, New Caledonia. *Journal of Metamorphic Geology* **20**, 151–165.

Matsumoto, K. & Hirajima, T. (2005). The coexistence of jadeite and omphacite in an eclogite-facies metaquartz diorite from the southern Sesia Zone, Western Alps, Italy. *Journal of Mineralogical and Petrological Sciences* **100**, 70–84.

Messiga, B., Kienast, J. R., Rebay, G., Riccardi, M. P. & Tribuzio, R. (1999). Cr-rich magnesiochloritoid eclogite from the Monviso ophiolites (Western Alps, Italy). *Journal of Metamorphic Geology* **17**, 287–299.

Miyazoe, T., Nishiyama, T., Uyeta, K., Miyazaki, K. & Mori, Y. (2009). Coexistence of pyroxenes jadeite, omphacite, and diopside/hedenbergite in an albite–omphacite rock from a serpentinite mélange in the Kurosegawa Zone of Central Kyushu, Japan. *American Mineralogist* **94**, 34–40.

Molina, J. F. & Poli, S. (2000). Carbonate stability and fluid composition in subducted oceanic crust: an experimental study on H_2O–CO_2-bearing basalts. *Earth and Planetary Science Letters* **176**, 295–310.

Morimoto, N., Fabries, J., Ferguson, A. K., Ginzburg, I. V., Ross, M., Seifert, F. A., Zussman, J., Aoki, K. & Gottardi, G. (1988). Nomenclature of pyroxenes. *American Mineralogist* **73**, 1123–1133.

Nadeau, S., Philippot, P. & Pineau, F. (1993). Fluid inclusion and mineral isotopic compositions (H–C–O) in eclogitic rocks as tracers of local fluid migration during high-pressure metamorphism. *Earth and Planetary Science Letters* **114**, 431–448.

Newton, R. C., Charlu, T. V. & Kleppa, O. J. (1980). Thermochemistry of the high structural state plagioclases. *Geochimica et Cosmochimica Acta* **44**, 933–941.

Okamoto, K. & Maruyama, S. (1999). The high-pressure synthesis of lawsonite in the MORB + H_2O system. *American Mineralogist* **84**, 362–373.

Parkinson, I. J. & Arculus, R. J. (1999). The redox state of subduction zones: insights from arc peridotites. *Chemical Geology* **160**, 409–423.

Pawley, A. R. & Holloway, J. R. (1993). Water sources for subduction zone volcanism; new experimental constraints. *Science* **260**, 664–667.

Peacock, S. M. (1993). The importance of blueschist–eclogite dehydration reactions in subducting oceanic crust. *Geological Society of America Bulletin* **105**, 684–694.

Peacock, S. M. & Wang, K. (1999). Seismic consequences of warm versus cool subduction zone metamorphism: Examples from northeast and southwest Japan. *Science* **286**, 937–939.

Peslier, A. H., Luhr, J. F. & Post, J. (2002). Low water contents in pyroxenes from spinel-peridotites of the oxidized, sub-arc mantle wedge. *Earth and Planetary Science Letters* **201**, 69–86.

Philippot, P. (1988). Déformation et éclogitisation progressives d'une croûte océanique subductée (Le Monviso, Alpes occidentales): contraintes cinématiques durant la collision alpine. PhD Thèse, University of Montpellier, 269 p.

Philippot, P. & Selverstone, J. (1991). Trace-element-rich brines in eclogitic veins: implications for fluid composition and transport during subduction. *Contributions to Mineralogy and Petrology* **106**, 417–430.

Pognante, U. (1985). Coronitic reactions and ductile shear zones in eclogitized ophiolite metagabbro, western Alps, north Italy. *Chemical Geology* **50**, 99–109.

Pognante, U. & Kienast, J.-R. (1987). Blueschist and eclogite transformations in Fe–Ti gabbros: a case from the western Alps ophiolites. *Journal of Petrology* **28**, 271–292.

Pognante, U. & Toscani, L. (1985). Geochemistry of basaltic and gabbroid metaophiolites from the Susa Valley, Italian Western Alps. *Schweizer Mineralogische und Petrographische Mitteilungen* **65**, 265–277.

Pognante, U., Lombardo, B. & Venturelli, G. (1982). Petrology and geochemistry of Fe–Ti gabbros and plagiogranites from the Western Alps Ophiolites. *Schweizer Mineralogische und Petrographische Mitteilungen* **62**, 457–472.

Poli, S. & Schmidt, M. W. (1995). H_2O transport and release in subduction zones—experimental constraints on basaltic and andesitic systems. *Journal of Geophysical Research* **100**, 22299–22314.

Poli, S., Franzolin, E., Fumagalli, P. & Crottini, A. (2009). The transport of carbon and hydrogen in subducted oceanic crust: an experimental study to 5 GPa. *Earth and Planetary Science Letters* **278**, 350–360.

Pouchou, J. L. & Pichoir, F. (1988). Determination of mass absorption coefficients for soft X-Rays by use of the electron microprobe. In: Newbury, E.D. (ed.) *Microbeam Analysis*. San Francisco, CA: San Francisco Press, pp. 319–324.

Powell, R. & Holland, T. J. B. (2008). On thermobarometry. *Journal of Metamorphic Geology* **26**, 155–179.

Proyer, A., Dachs, E. & McCammon, C. (2004). Pitfalls in geothermobarometry of eclogites: Fe^{3+} and changes in the mineral chemistry of omphacite at ultrahigh pressures. *Contributions to Mineralogy and Petrology* **147**, 305–318.

Rossetti, P. & Ferrero, S. (2008). The Zn–Pb deposits of Casario (Ligurian Alps, NW Italy): late Palaeozoic sedimentary–exhalative bodies affected by the alpine metamorphism. *Geodinamica Acta* **21**, 117–137.

Rowe, M. C., Kent, A. J. R. & Nielsen, R. L. (2009). Subduction influence on oxygen fugacity and trace and volatile elements in basalts across the Cascade Volcanic Arc. *Journal of Petrology* **50**, 61–91.

Royden, L. H. & Husson, L. (2006). Trench motion, slab geometry and viscous stresses in subduction systems. *Geophysical Journal International* **167**, 881–905.

Rubatto, D. & Hermann, J. (2003). Zircon formation during fluid circulation in eclogites (Monviso Western Alps): implications for Zr and Hf budget in subduction zones. *Geochimica et Cosmochimica Acta* **67**, 2173–2187.

Rüpke, L. H., Morgan, J. P., Hort, M. & Connolly, J. A. D. (2004). Serpentine and the subduction zone water cycle. *Earth and Planetary Science Letters* **223**, 17–34.

Schellart, W. P., Freeman, J., Stegman, D. R., Moresi, L. & May, D. (2007). Evolution and diversity of subduction zones controlled by slab width. *Nature* **446**, 308–311.

Schmid, R., Wilke, M., Oberhänsli, R., Janssens, K., Falkenberg, G., Franz, L. & Gaab, A. (2003). Micro-XANES determination of ferric iron and its application in thermobarometry. *Lithos* **70**, 381–392.

Schmidt, M. W. & Poli, S. (1998). Experimentally based water budgets for dehydrating slabs and consequences for arc magma generation. *Earth and Planetary Science Letters* **163**, 361–379.

Schwartz, S., Lardeaux, J.-M., Guillot, S. & Tricart, P. (2000). Diversité du métamorphisme éclogitique dans le massif ophiolitique du Monviso (Alpes occidentales, Italie). *Geodinamica Acta* **13**, 169–188.

Sobolev, V. N., McCammon, C. A., Taylor, L. A., Snyder, G. A. & Sobolev, N. V. (1999). Precise Mössbauer milliprobe determination of ferric iron in rock-forming minerals and limitations of electron microprobe analysis. *American Mineralogist* **84**, 78–85.

Spandler, C., Hermann, J., Arculus, R. & Mavrogenes, J. (2004). Geochemical heterogeneity and element mobility in deeply subducted oceanic crust: insights from high pressure mafic rocks from New Caledonia. *Chemical Geology* **206**, 21–42.

Štípská, P. & Powell, R. (2005). Constraining the *P–T* path of a MORB-type eclogite using pseudosections, garnet zoning and garnet–clinopyroxene thermometry: an example from the Bohemian Massif. *Journal of Metamorphic Geology* **23**, 725–743.

Stüwe, K. (1997). Effective bulk composition changes due to cooling: a model predicting complexities in retrograde reaction textures. *Contributions to Mineralogy and Petrology* **129**, 43–52.

Tsujimori, T., Liou, J. G. & Coleman, R. G. (2005). Coexisting retrograde jadeite and omphacite in a jadeite-bearing lawsonite eclogite from the Montagua Fault Zone, Guatemala. *American Mineralogist* **90**, 836–842.

Tsujimori, T., Sisson, V. B., Liou, J. G., Harlow, G. E. & Sorensen, S. S. (2006*a*). Petrologic characterization of Guatemalan lawsonite-eclogite: eclogitization of subducted oceanic crust in a cold subduction zone. In: Hacker, B. H., McClelland, W. C. & Liou, J. G. (eds) *Ultrahigh-pressure Metamorphism: Deep Continental Subduction. Geological Society of America, Special Papers* **403**, 127–138.

Tsujimori, T., Sisson, V. B., Liou, J. G., Harlow, G. E. & Sorensen, S. S. (2006*b*). Very-low-temperature record of the subduction process: a review of worldwide lawsonite eclogites. *Lithos* **92**, 609–624.

Vidal, O., De Andrade, V., Lewin, E., Munoz, M., Parra, T. & Pascarelli, S. (2006). *P–T*–deformation–Fe^{3+}/Fe^{2+} mapping at the thin section scale and comparison with XANES mapping: application to a garnet-bearing metapelite from the Sambagawa metamorphic belt (Japan). *Journal of Metamorphic Geology* **24**, 669–683.

Warren, C. J. & Waters, D. J. (2006). Oxidized eclogites and garnet-blueschists from Oman: *P–T* path modelling in the NCFMASHO system. *Journal of Metamorphic Geology* **24**, 783–802.

Wei, C. J., Powell, R. & Zhang, L. F. (2003). Eclogite from the southern Tianshan, NW China: petrological characteristic and calculated mineral equilibria in the Na_2O–CaO–FeO–MgO–Al_2O_3–SiO_2–H_2O system. *Journal of Metamorphic Geology* **21**, 163–179.

Wei, C. J., Yang, Y., Su, L., Song, S. G. & Zhang, L. F. (2009). Metamorphic evolution of low-*T* eclogite from the North Qilian orogen, NW China: evidence from petrology and calculated phase equilibria in the system NCKFMASHO. *Journal of Metamorphic Geology* **27**, 55–70.

White, R. W., Powell, R. & Holland, T. J. B. (2007). Progress relating to calculation of partial melting equilibria for metapelites. *Journal of Metamorphic Geology* **25**, 511–527.

Will, T. M., Okrusch, M., Schmädicke, E. & Chen, G. (1998). Phase relations in the greenschist–blueschist–amphibolite–eclogite facies in the system Na_2O–CaO–FeO–MgO–Al_2O_3–SiO_2–H_2O (NCFMASH), with applications to the *PT*-evolution of metamorphic rocks from Samos, Greece. *Contributions to Mineralogy and Petrology* **32**, 85–102.

Wood, B. J., Bryndzia, L. T. & Johnson, K. E. (1990). Mantle oxidation state and its relationship to tectonic environment and fluid speciation. *Science* **248**, 337–345.

Yaxley, G. M. & Green, D. H. (1994). Experimental demonstration of refractory carbonate bearing eclogite and siliceous melt in the subduction regime. *Earth and Planetary Science Letters* **128**, 313–325.

Zuluaga, C. A., Stowell, H. & Tinkham, D. (2005). The effect of zoned garnet on metapelite pseudosection topology and calculated metamorphic *P–T* paths. *American Mineralogist* **90**, 1619–1628.

APPENDIX A: ANALYTICAL METHODS

Mineral chemistry

The rock-forming minerals were analysed using both SEM–EDS and electron-microprobe analyser (EMPA)–wavelength-dispersion spectrometry (WDS). A Cambridge Stereoscan 360 SEM equipped with an EDS Energy 200 and a Pentafet detector (Oxford Instruments) was used at the Department of Mineralogical and Petrological Sciences, University of Torino (Italy) with the following operating conditions: 50 s counting time and 15 kV accelerating voltage. SEM-EDS quantitative data (spot size = 2 μm) were acquired and processed using the Microanalysis Suite Issue 12, INCA Suite version 4.01; the raw data were calibrated on natural mineral standards and the ΦρZ correction (Pouchou & Pichoir, 1988) was applied. Qualitative EDS elemental maps (Fig. 3) were acquired using a 15 kV accelerating potential, a very short dwell time of 120 ms (corresponding to an acquisition time of *c.* 12 h, including a detector dead time *c.* 30%) and at a resolution of 512 × 512 pixels. A JEOL 8200 Superprobe (WDS) was used at the Department of Earth Sciences, University of Milano (Italy). Acceleration voltage was set to 15 kV, beam current was 15 nA and natural minerals were used as standards. A ΦρZ routine was used for matrix correction.

$Fe^{3+}/\Sigma Fe$ estimates in garnet and omphacite

The $Fe^{3+}/\Sigma Fe$ ratio of garnet was measured by electron microprobe using the 'flank method' (Höfer *et al.*, 1994; Höfer & Brey, 2007) calibrated on the JEOL 8200 Superprobe at the Department of Earth Sciences, University of Milano (Malaspina *et al.*, 2009). Combined 'flank method' and quantitative elemental analysis were performed on wavelength-dispersive spectra at 15 kV and 60 nA. One spectrometer with a TAP crystal and 300 μm slit was used for the 'flank method', measuring the FeLβ and FeLα at a counting time of 300 s (Fig. SM3c, Supplementary Material). With the remaining four spectrometers Si, Ti, Al, Cr, Fe, Mg, Mn and Ca were measured simultaneously. The quantitative $Fe^{3+}/\Sigma Fe$ in garnets was determined by applying the correction for self-absorption (see Höfer & Brey, 2007, for details), using natural and synthetic garnet end-members with fixed $Fe^{3+}/\Sigma Fe$ as standards (Malaspina *et al.*, 2009). Mineral analyses were always performed using detailed back-scattered electron images to check the microtextural site. The accuracy of the 'flank method' has been demonstrated in previous studies, where an error between ± 0·02 and ± 0·04 for $Fe^{3+}/\Sigma Fe$ has been documented in samples with 8–11 wt % total Fe (Höfer & Brey, 2007).

The $Fe^{3+}/\Sigma Fe$ ratios of pyroxenes were calculated assuming stoichiometry and four cations based on six oxygen atoms; the classification of Morimoto *et al.* (1988) was used. The calculated $Fe^{3+}/\Sigma Fe$ ratios do not change using the method of Matsumoto & Hirajima (2005), which considers $Fe^{3+} = Na - {}^{VI}Al_{Jd}$ [for Si >2·00, ${}^{VI}Al_{Jd} = Al_{tot}$; for Si <2·00, ${}^{VI}Al_{Jd} = Al_{tot} - 2^{IV}Al$ and ${}^{IV}Al = 2 - Si$].

Bulk-composition calculation by combining mineral modes and compositions

Qualitative major element X-ray maps of a representative portion of the thin section (*c.* 8 mm × 6 mm) were acquired using a μ-XRF Eagle III-XPL spectrometer equipped with an EDS Si(Li) detector and with an Edax Vision32 microanalytical system, located at the Department of Mineralogical and Petrological Sciences, University of Torino. The operating conditions were: 400 ms counting time, 40 kV accelerating voltage and a probe current of 800 μA. A spatial resolution of about 30 μm in both *x* and *y* directions was used; the spot size was *c.* 30 μm. Quantitative modal amounts of each mineral phase were obtained by processing the μ-XRF maps with the software program Petromod (Cossio *et al.*, 2002) (Fig. SM2, Supplementary Material). The bulk-rock composition of sample OF2727 was then calculated by combining the mineral proportions obtained from the modal estimate of the micro-XRF maps with the mineral chemistry acquired by SEM-EDS (Table SM1, Supplementary Material).

APPENDIX B: DETAILS ON THE PSEUDOSECTIONS CALCULATION

The evolution of metagabbro OF2727 was modelled in the system MnNCFMASHTO. A fluid phase, assumed to be pure H_2O, was considered to be in excess because water saturation is essential to consider lawsonite stability (Clarke *et al.*, 2006). K_2O was not considered in the calculation because of its very low content in the bulk composition.

Pseudosections were calculated following the approach of Connolly (1990, 2009) (Perple_X version 08), using the internally consistent thermodynamic dataset and equation of state for H_2O of Holland & Powell (1998, revised 2004). The minerals considered in the calculation were: garnet, omphacite, chlorite, amphibole, lawsonite, talc, epidote, paragonite, quartz, rutile, ilmenite, titanite and magnetite. The following solid-solution models were used: garnet and

epidote (Holland & Powell, 1998), omphacite (Green *et al.*, 2007), chlorite (Holland *et al.*, 1998), amphibole (Diener *et al.*, 2007), plagioclase (Newton *et al.*, 1980) and talc (ideal model). Pumpellyite was not included in the calculation because its stability is limited to $T < 350^{\circ}C$ and $P < 8$ kbar (e.g. Rossetti & Ferrero, 2008); that is, at P–T conditions not considered in the modelling.

APPENDIX C: DETAILS ON THE CALCULATIONS OF DEHYDRATION AND REDOX REACTIONS

The dehydration equilibria occurring within the quinivariant field Lws + Qtz + Chl + Omp + Grt + Rt of the pseudosection reported in Fig. 5b were recalculated (Fig. 8) for composition 1e in the system NCFMASHTO, using the same solution models as in Fig. 5. In this case, however, the spessartine and amesite end-members were not included in the solution models, because of the very low content of these end-members in garnet and chlorite, respectively. This approximation was also required because the new pseudosection of Fig. 8 was the starting point for modelling the redox equilibria in the T–log $f(O_2)$ projection of Fig. 9 and an exact correspondence between the two grids was needed. Simplification of the solid-solutions in the modelling of redox equilibria reduces the number of pseudocompounds (and thus the number of calculated equilibria) and avoids numerical overflow. As a consequence of this simplification, the garnet-in and lawsonite-out curves are shifted up-T and down-T by 20°C and 15°C, respectively, at constant P (compare Fig. 5b and Fig. 8).

APPENDIX D: SUPPLEMENTARY MATERIAL

Supplementary Material includes: (1) representative microstructures in the studied sample OF2727 compared with those of two other FeTi-oxide metagabbros from the same area (Fig. SM1); (2) the processed μ-XRF map used for the modal estimate of the phase proportions (Fig. SM2); (3) additional compositional profiles for garnet and information from the flank method used to estimate the $Fe^{3+}/\Sigma Fe$ ratio (Fig. SM3); (4) the comparison between the bulk composition of sample OF2727 and other metagabbros from the Western Alps (Fig. SM4); (5) some details on the method used to calculate the effects of chemical fractionation on the bulk composition owing to the growth of zoned garnet (Fig. SM5); (6) a set of P–T pseudosections for stages I and II (1a, 1e, 2a and 2c) with compositional isopleths of garnet and omphacite, calculated at various $X(Fe_2O_3)$ values and used for the $X(Fe_2O_3)$ estimate (Fig. SM6a and b); (7) the complete set of P–T pseudosections for stages I and II (1a–1e, 2a–2c), calculated at $X(Fe_2O_3) = 0{\cdot}20$ and 0·15 respectively, with compositional isopleths of garnet and omphacite (Fig. SM7a–d); (8) a table showing the bulk composition of sample OF2727 estimated from mineral modes and compositions (Table SM1).